Kästner, Marcus; Rangelow, Ivo W.:

Scanning probe lithography on calixarene towards single-digit nanometer fabrication

Original published in:	International journal of extreme manufacturing. - Bristol : IOP Publishing. - 2 (2020), 3, art. 032005, 21 pp.
Original published:	2020-08-04
ISSN:	2631-7990
DOI:	10.1088/2631-7990/aba2d8
[*Visited:*	2020-11-09]

OPEN ACCESS
IOP Publishing | IMMT
International Journal of Extreme Manufacturing
Int. J. Extrem. Manuf. **2** (2020) 032005 (21pp)
https://doi.org/10.1088/2631-7990/aba2d8

Scanning probe lithography on calixarene towards single-digit nanometer fabrication

Marcus Kaestner and Ivo W Rangelow

Institute of Micro- and Nanoelectronics, Nanoscale Systems Group, Faculty of Electrical Engineering and Information Technology, Ilmenau University of Technology, Gustav-Kirchhoff-Str. 1, 98693 Ilmenau, Germany

E-mail: ivo.rangelow@tu-ilmenau.de

Received 12 March 2020, revised 10 June 2020
Accepted for publication 2 July 2020
Published 4 August 2020

Abstract

Cost effective patterning based on scanning probe nanolithography (SPL) has the potential for electronic and optical nano-device manufacturing and other nanotechnological applications. One of the fundamental advantages of SPL is its capability for patterning and imaging employing the same probe. This is achieved with self-sensing and self-actuating cantilevers, also known as 'active' cantilevers. Here we used active cantilevers to demonstrate a novel path towards single digit nanoscale patterning by employing a low energy (<100 eV) electron exposure to thin films of molecular resist. By tuning the electron energies to the lithographically relevant chemical resist transformations, the interaction volumes can be highly localized. This method allows for greater control over spatially confined lithography and enhances sensitivity. We found that at low electron energies, the exposure in ambient conditions required approximately 10 electrons per single calixarene molecule to induce a crosslinking event. The sensitivity was 80-times greater than a classical electron beam exposure at 30 keV. By operating the electro-exposure process in ambient conditions a novel lithographic reaction scheme based on a direct ablation of resist material (positive tone) is presented.

Keywords: nanofabrication, field-emission scanning probe lithography, single nanometer lithography, molecular resist

(Some figures may appear in colour only in the online journal)

1. Introduction

Today's lithography methods are based on particles (e.g. atoms, electrons, ions, and photons), thermo-mechanical molding (imprint) of polymers, and tip-based interactions. Every kind of lithography owns its specific characteristics, advantages, and disadvantages—however, reason to exist for one or many dedicated applications is based on dedicated criteria for choice of a particular lithographic technique. The industry requirements for mass production are focused on lithographic performance, most importantly achieving high throughput at minimal resolution and forcing capital resources without restriction.

Among the predicted lithographic technologies that could be further developed, tip-based methods combined with established high-throughput techniques (e.g. optical lithography in a so called mix and match approach) could be a cost effective candidate for manufacturing sub-5 nm NIL-templates, masks, and highly customized and tailored nanoelectronics, which are not necessarily focused on throughput.

The further technological road points towards single electron or atomic-scale devices [1]. These visions are currently beyond our capabilities. The main restriction is the

2631-7990/20/032005+21$33.00

lack of cost-effective and rapid prototyping manufacturing processes, which deliver routine features at the single digit nano scale. The demands of next generation lithographic technologies with respect to resolution capabilities, overlay alignment accuracy, process control, and throughput constitutes an overall bottleneck.

The following interactions can be triggered for nanopatterning within a spatially well-defined region surrounding the tip:

(i) Force-induced interactions such as plowing [2], nanoshaving, and nanografting [3],
(ii) Heat-induced thermomechanical [4] or thermochemical [5] interactions.
(iii) Electric-field-induced interactions, such as material deposition by field-induced deposition/decomposition of gaseous precursors [6].
(iv) Material displacement using joule heating induced by electrostatic SPL [7].
(v) Material modification by spatially confined anodic oxidation reactions [8].
(vi) Resist exposure using field-emitted low-energy electrons [9].
(vii) Material removal by electric-field- and/or current-induced interactions and field emission-scanning probe lithography (FE-SPL) [10].

In standard electron beam lithography (EBL), wherein high-energy primary electron beams (5–100 keV) are applied, electrons pass through a resist undergoing a series of elastic and inelastic scattering events, generating secondary electrons (SE), backscattered electrons (BSE), plasmons, phonons, and photons beyond the primary impact point of the initial beam [11–18]. The sum of all events contributes to the deposited energy in the resist. The final geometry of the feature is defined by the sum of all voxels at which the threshold for the lithographic reaction is exceeded. Thereby, proximity effects, which are defined by forward and backward scattering, laterally extends the interaction far beyond the initial exposure spot. Tenths of nanometers (forward scattering) up to several micrometers (backward scattering) are typical proximity ranges [12, 15–18].

To push the resolution limits of EBL towards the single digit nano scale, highly accelerated primary beams with energies of 100–350 keV were used. In conjunction with thin resist layers, which were coated on top of membrane samples, Manfrinato *et al* wrote 2 nm isolated and 5 nm half-pitch (hp) features [16]. They eliminated long-range backward scattering by applying a dedicated membrane substrate combined with very thin resist layers. Using high-energy beams minimized forward scattering and related SE emission. However, the use of this technology for practical applications is not straight-forward. In the case of bulk samples, the relatively large inelastic mean free path (IMFP) of high-energy electrons causes the energy to deposit in the bulk rather than in the resist layer [12]. This energy mismatch significantly decreases the exposure efficiency and increases the likelihood of radiation damage and substrate heating [11, 16].

Low-energy electron beam lithography provides an alternative pathway towards high-resolution sub-5 nm lithography. At low-electron energies, the IMFP is reduced, leading to decreased penetration volumes of the electrons itself [12–19]. The primary electrons deposit nearly their entire energy within the resist layer. As demonstrated for PMMA, primary electrons penetrate an average resist thickness of >14 μm at 30 keV, whereas at 1 keV an incident electron beam cannot completely expose a 50 nm thick film [19–21]. Here, an experimental relationship between penetration depth d_p and incident energy E_e was found with $d_p \sim E_e^{1,6\pm0,35}$ [22].

As shown, the loss of energy is proportional to $1/Ee$, valid for a certain energy range >100 eV. For energies below ~100 eV in PMMA and Carbon, the stopping power typically decreases with decreasing energy [23, 24].

Additionally, Wu and Neureuther pointed out that 90% of SEs with energies of <400 eV travel less than 12 nm in PMMA, while SEs with energies of <200 eV have a travel range of less than 5 nm [21]. Thus, the majority of electrons scatter within the resist film. The spatial resolution is defined by the primary beam and the induced SEs [25]. This reduces backscattering, suppresses radiation damage and heating effects, and improves exposure efficiency and sensitivity of the resist [14, 18, 21, 25].

However, the progress towards the 5 nm scale reveals another limitation: The macromolecular resist characteristics [26, 27]. Initial efforts have been made by using calixarene molecular glass resists and its derivate in EBL [28]. Fujita *et al* [28] first demonstrated that calixarene behaves as a high-resolution negative tone resist. Later, fine isolated features with a width of 8 nm were shown within chloromethyl-methoxy-calix[4]arene resist thin films using 50 keV electron exposure [29]. Recently, Solak *et al* demonstrated 12.5 nm hp resolution capabilities of calixarene in EUV interference lithography [30]. A drawback of the small size and low molecular weight of the resist system is that it requires more crosslinks per unit volume in order to induce a solubility change [31]. Compared to PMMA, crosslinking a calixarene-based resist requires a 20-times larger area [28]. This general trend of decreasing sensitivity with decreasing molecular weight was revealed by Charlesby for polymeric resists [32]. The latter was reported by Perkins *et al* [33] for chemically amplified resist systems (CAR's) as well as by Wilder *et al* [34, 35] for polymeric resists, such as SAL601 and PMMA. These findings contradict the initial theory of low-energy electron exposure, leading to the assumption that low-energy FE-SPL involves fundamentally different mechanisms (see [33, 34]). Experiments by Ruderisch [36] and Sailer [37] pointed out that the aromatic systems are partially broken and the oxidation state of the carbon atoms, at which the phenolic hydroxyl group was originally bound, are raised. In general, no defined final state could be found by spectroscopic investigations. Instead, they observed an increase in chemical heterogeneity, which suggests that no defined final state of the crosslinked molecules was present and multiple mechanisms were triggered by the incident radiation. Sailer suggested that partial oxidation of the molecular structure is most likely [37]. Prins *et al* [38] concluded the main mechanism involved a break-up of arenes with respective subsequent linking to other arenes or functional

groups. Laser-based dry development experiments combined with EBL on calixarene, carried out by Olynick *et al*, suggested the formation of aromatic OH followed by aromatic OH_2+ [39, 40]. The laser-triggered ablation process was promoted by the inter-play of phenolic units and extended conjugation in the aromatics [40].

Sub-10 nm lithography for a production environment is not considered realistic with currently available lithographic equipment. Standard optical lithography features the high throughput demand needed, but meeting high resolution demands becomes extremely challenging and expensive. In contrast, advanced technologies with sufficient capabilities for sub-5 nm [41] processing such as direct write e-beam are extremely expensive and lack throughput. A mix and match lithography approach combines the advantages of both worlds using a convectional exposure technique for all noncritical levels and a scanning probe system for critical levels [41, 42].

This paper begins by explaining the findings behind the principle of exposure with low-energy electrons using a scanning probe for exposure of a molecular glass resist (calaxirene) and summarizes our efforts to develop a novel lithographic strategy. This paper presents scanning probe lithography as an original mechanism for fabricating sub-5 nm [41] negative and positive tone. The second section covers the set-up of the scanning probe lithography based on so called 'active' cantilevers (i.e. cantilevers with integrated bending readout and actuator). The exposure mechanisms with low energy electrons and the relation between exposure dose and lithographic tone are presented in the third section. The fourth section discusses the effect of the exposure-environment where we present the effects of relative ambient humidity and resist-surface degradation. The environment effect is demonstrated by experiments provided at ambient humidity/temperature and vacuum. The evidence proves that OH groups were involved in the formation of positive and negative tone. This paper concludes with a discussion of the results.

2. The principle of exposure with low-energy electrons using a scanning probe

The energy of the electron determines its average travel length within a specific material (i.e. mean free path of the electron). The minimum mean free path ranges between 10 to 100 eV and increases towards higher and lower energies. Since secondary electrons dominate the reactions for exposure of resist or precursor molecules, their relatively long mean free path can contribute to image blur and loss of resolution in the final pattern. Therefore, the electron energy significantly impacts spatial resolution in electron-based lithography. Electrons with energies below 100 eV constitute the majority of secondary electrons (SE), which are primarily responsible for the lithographic interactions in conventional EBL. The SE distribution is characterized by a large low-energy peak at <50 eV. As predicted by established theories, the energy transfer between incident electrons with low energies, in a specific energy range depending on the resist and underlying lithographic reaction, is expected be more efficient.

Here, the associated electron energies are very close to lithographic relevant excitations, which are predominantly bond scission processes [12, 13, 28, 43, 44]. According to Vriens law, the lithographically relevant exposure reaction cross-sections have maxima at 8–12 eV for typical binding strengths of C–C and O–H chemical bonds [45, 46]. The increased cross-sections at low energies (1–20 eV) were experimentally proven for certain organic molecules, such as CH_4 and substituted benzenes [35, 47, 48]. Ionization effects appeared irrelevant for electron energies $\leqslant$50 eV. Electron-impact ionization cross-sections have maxima at higher energetic ranges—for typical organic resist compounds these are located above 70 eV [49]. The high stopping power at low energies indicated a high inelastic scattering cross-section and low inelastic scattering mean free path. According to basic investigations of these phenomena [50–53], we can conclude that there is high inelastic scattering. The scattering is spatially confined, which significantly reduces the proximity effect.

Thus, the energy for the lithographic reaction can be better confined towards a few angstroms radially around the incident beam [12].

There have been some attempts to access the low energy exposure regime by miniaturized EBL columns or retarding electron optics [54–56]. However, the construction of such systems with small spot sizes is challenging to achieve using established electron-optical designs. A different approach for lithographic purposes constitutes the utilization of a proximal probe setup using an active cantilever system [10, 42]. This kind of setup is schematically outlined in figure 1 (extended cantilever) and FE-SPL system description provided in [57–59]. In standard EBL the electron beam is generated, conditioned, blanked, and focused relatively far away from the sample surface by a complex electron optical system under high-vacuum conditions.

In contrast, the exposure situation in FE-SPL is quite different:

(i) Due to the field-enhancement effect at the tip apex, only small voltages (typ. range of 10–100 V) between the sharp tip and sample are required in order to stimulate a Fowler–Nordheim (FN) field emission [60, 61]. The radius of the tip apex usually ranges between 7 to 15 nm [26–28]. The corresponding emission characteristics were measured by a voltage (U) sweep, while the tip-sample spacing was held constant (tip-sample spacing d of ~20–40 nm). The respective FN-emission, shown for a particular sample in figure 2, exhibits a linear dependency between $\ln(I/U^2)$ vs. 1/U after the onset of emission (at U ~ 15 V). This confirms a stable electron emission process at ambient conditions in the Fowler–Nordheim [60] regime. This result corresponds with early stage STM exposure experiments [34, 62].

(ii) The exposure dose in FE-SPL is controlled by the emission current and the tip velocity in the. case of vector-based line patterning or by the dwell time in the case of single pixel/-dot patterning.

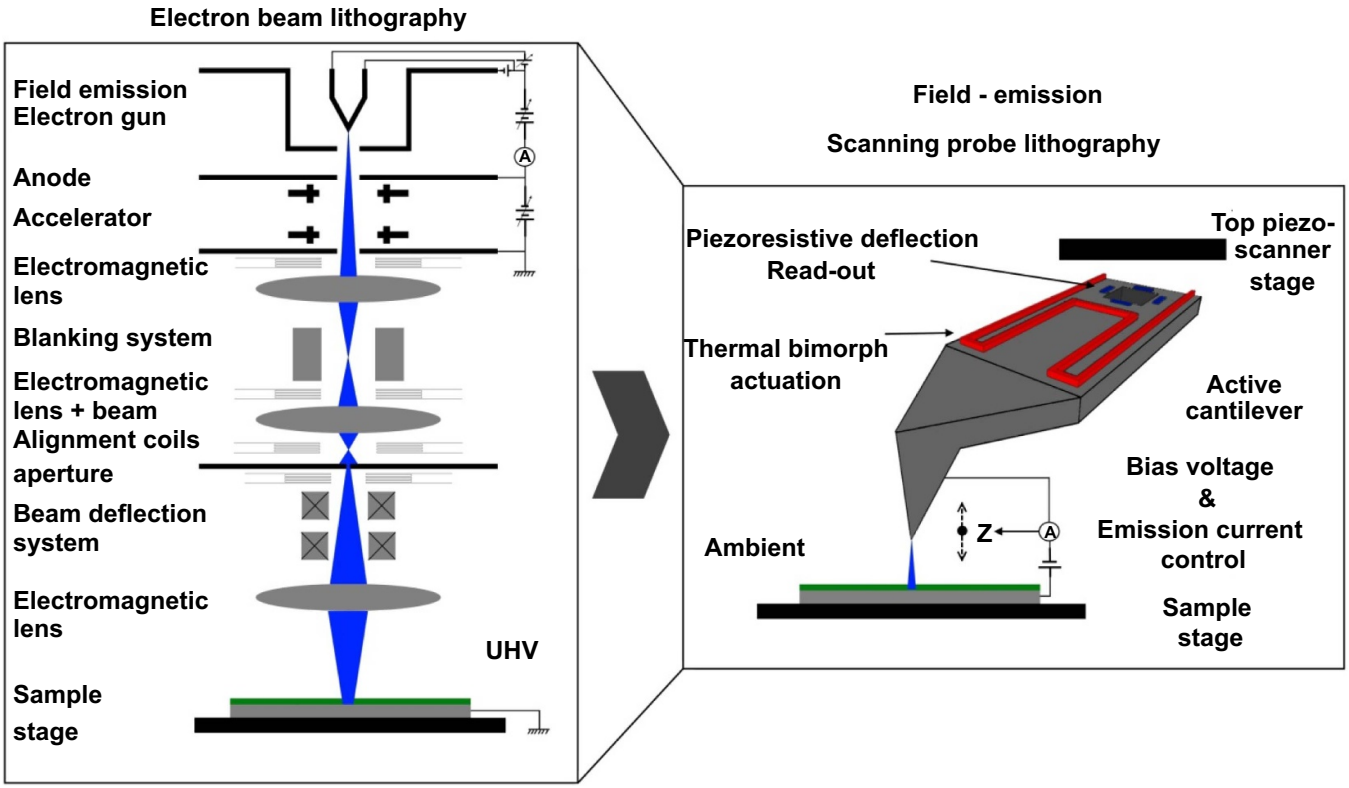

Figure 1. From classical electron beam lithography (EBL) towards a novel field-emission scanning probe lithography (FE-SPL) system with so called 'active' cantilever. These cantilevers are equipped with piezoresistive bending senor, a thermomechanical actuator and a sharp tip. In this manner, lithography and imaging are employed using the same cantilever.

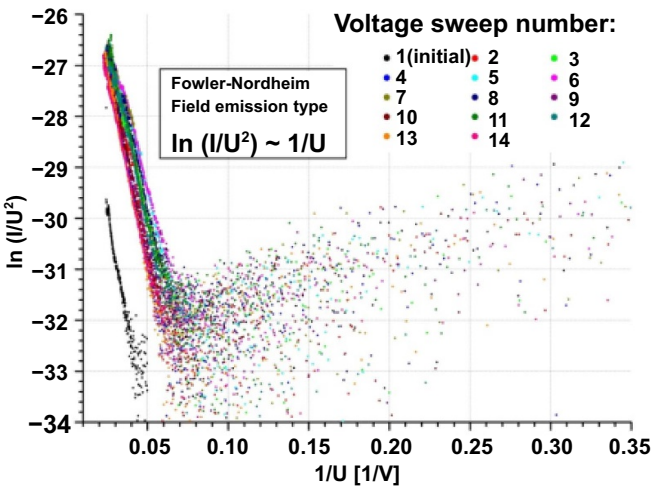

Figure 2. Fowler–Nordheim (FN) plot of a field emission measurement carried out with a sharp tungsten tip. The tip is in close proximity to a pristine Cr/Au coated sample. The experiment was performed in ambient conditions. The different colors, numbered 1–14, correspond to successive voltage sweeps of the same tip. The offset between the initial voltage sweep (#1, black dots) and the subsequent measurements (#2–14) are attributed to tip contaminations, which were removed after the initial sweep.

Thereby, the system's feedback loop maintains a constant emission current by controlling the tip-sample spacing (in figure 1 marked by Z). In this way, constant electric field strength at the tip apex is achieved. The tip-sample emission current is measured by a highly sensitive IU-converter and amplification stage (RMS noise floor < 100 fA at 1 kHz bandwidth). The noise and regulation system limit is determined with a minimum exposure dose of 1.9 fC in the case of spot exposure and 2 nC cm^{-1} in line exposure, respectively.

(iii) A linear relationship between applied bias and tip-sample spacing (figure 1) confirms the general operation in the Fowler–Nordheim regime [60]. Thus, depending on the thickness of the resist, a minimum bias voltage has to be applied to prevent mechanical tip-resist interactions.

(iv) Since the tip-surface distance is significantly smaller than the mean free path (MFP) of the electrons in ambient conditions (~340–570 nm [63–66]), vacuum conditions are not required.

(v) The application of low energy electrons < 100 eV, which enlarge the de Broglie wavelength (30 eV → 0.224 nm vs. 30 keV → 0.007 nm), do not affect resolution in lithographic applications.

(vi) Due to the low energy operation, the electrons' IMFP is drastically reduced, ranging between 1 to a few nanometers, within the resist layer, concluded from [11–13, 43, 44, 66, 67]. In addition, a typical reaction depth of 1–3 nm for 50–100 eV electrons is estimated [22, 66, 68]. The IMFP in a low-energy operation is typically smaller than the applied resist thickness. In contrast, in standard EBL

the IMFP of the incident primary electrons is much larger than the resist layer thickness. This suggests that the low energy electrons cannot penetrate the complete resist thickness with their initial energy.

(vii) However, in the case of FE-SPL, the space between the electron emitter (tip apex) and the resist-coated sample surface is not field-free. The low energy electrons emitted from the nano-tip regain energy from the field after losing energy due to inelastic scattering events [12, 33–35, 69–73].

(viii) From a theoretical point of view, thermal effects can be excluded in FE-SPL. This is substantiated by calculations of Perkins *et al* [34], who investigated the low current operation range ($\leq$ 100 pA) for polymeric resist materials. As theoretically investigated by Lyuksyutov *et al*, a minimum current of 5–10 nA is required to soften PMMA and PS thin films [74]. The significant influence of the exposure environment supports the fact that chemical reaction pathways are triggered. Electromigration effects are not likely [75] in these conditions and were not observed in the exposure experiments conducted between a metallized tip and sample surface.

In conclusion, it is suggested that different mechanisms and chemical reaction schemes occur in FE-SPL. This assumption is supported by initial investigations of scanning probe induced resist exposure processes, which were carried out in the early stage of STM/AFM [19, 31–36, 41, 42]. In 2003 [10] and 2006 [26], Rangelow *et al* demonstrated the first positive tone self-development behavior of calixarene in low energy electron exposure. These result indicate the presence of different reaction paths.

As expected, the lithographic reaction in FE-SPL depends on the applied electron exposure dose. This observation is summarized in figure 3. L-shape meander line patterns were written with different line exposure doses into ~6 nm thick calixarene resist layers (cmc4r derivate), which were spin-coated on top of a Cr/Au bottom layer. Electrons with energies of 40 eV (=bias voltage) were emitted from a Ti/Pt coated cantilever tip (r_{tip} ~ 25 nm). In order to determine the impact of low energy electron exposure in ambient conditions, AFM topographic imaging was carried out directly after exposure. AFM and SEM inspection after a subsequent wet development (WD) step provides further information about the associated crosslinked resist material. A complete 2D section profile reveals the inner structure of the lithographically defined features within the resist material.

Different pattern types emerge, as a function of exposure dose and line pitch, as shown in figure 3.

In figure 3(i), low electron exposure doses induced a crosslinking process of the molecular glass resist. The involved chemical reactions rendered the exposed resist insoluble. A wet development step revealed the extension of the crosslinked area (colored in green), which appears as raised features. Well known negative tone behavior was observed.

In figure 3(ii), an increased exposure dose led to significant changes in lithographic reaction. The decrease in features was measured by AFM imaging directly after exposure. Thus, resist material was directly removed by the low-energy electron exposure process. We call this effect ablation. Since no development is required to make use of the generated features one can describe the lithographic interaction as self-development or development-less patterning. Derived from SEM contrast after wet development, we suppose that the entire resist material in the center of the lines was ablated, unveiling the Cr/Au bottom layer.[1] A wet development step revealed that the ablated lines were surrounded by crosslinked resist areas (colored in green).

A reduction of the line spacing (=line pitch) indicates an overlap of crosslinked side areas, whereas the directly ablated lines (positive tone features) resolved separately.

3. Set-up of the scanning probe lithography

Lithographic low-energy electron exposure at ambient conditions was conducted by a custom-built scanning probe lithography platform. The tool is described in ref. [41, 42].

The lithographic system was placed in a vibration-isolated, environmentally encapsulated chamber (figure 4). The environmental conditions were stabilized at 35% r.h. and ~ 25 °C. Active cantilevers were applied for standard closed loop scanning probe lithography, which incorporated imaging by standard AFM modes as well as low energy electron field emission lithography. Active cantilevers integrate both the actuation and the deflection read-out onto the cantilever beam itself, described in more detail in [57–59].

An actuator based on thermo-mechanical principles drives the cantilever on resonant oscillation (AC) and provides static deflection control (DC) (figure 5(a)). The deflection read-out was realized by integrating 2-DEG piezoresistive sensors based on p-doped Si in a Wheatstone-bridge configuration at the base of the cantilever in order to minimize temperature influences and deliver atomic resolution. The spring constants of the applied cantilever range between 90–100 N m^{-1}. A conductive diamond tip coated with either Ti/Pt or W was utilized as the proximal emission source of low-energy electrons in lithographic mode and for imaging the lithographic features in non-contact AFM-mode without removing the sample and carry out a development step (figure 5(b)).

In several previously published papers, we discussed the requirements and developments that contributed to new generation of scanning probes. We elaborated on the efforts toward downsizing self-sensed and self-actuated probes, their control and design approaches, and upscaling the cantilever [58]. We presented the fabrication process of active probes along with the tip customizations carried out targeting specific application fields [57–59, 64, 76]. Promising applications in the scope of

[1] Note: Since the penetration depth in AFM measurement is rather limited, especially for the small trenches created, one cannot doubtlessly conclude onto the depth of the ablated line. From SEM image contrast it seems to be scum-free opened to the bottom Cr/Au layer, whereas the AFM tip stops approx. 1.5–2.5 nm before reaching the bottom layer.

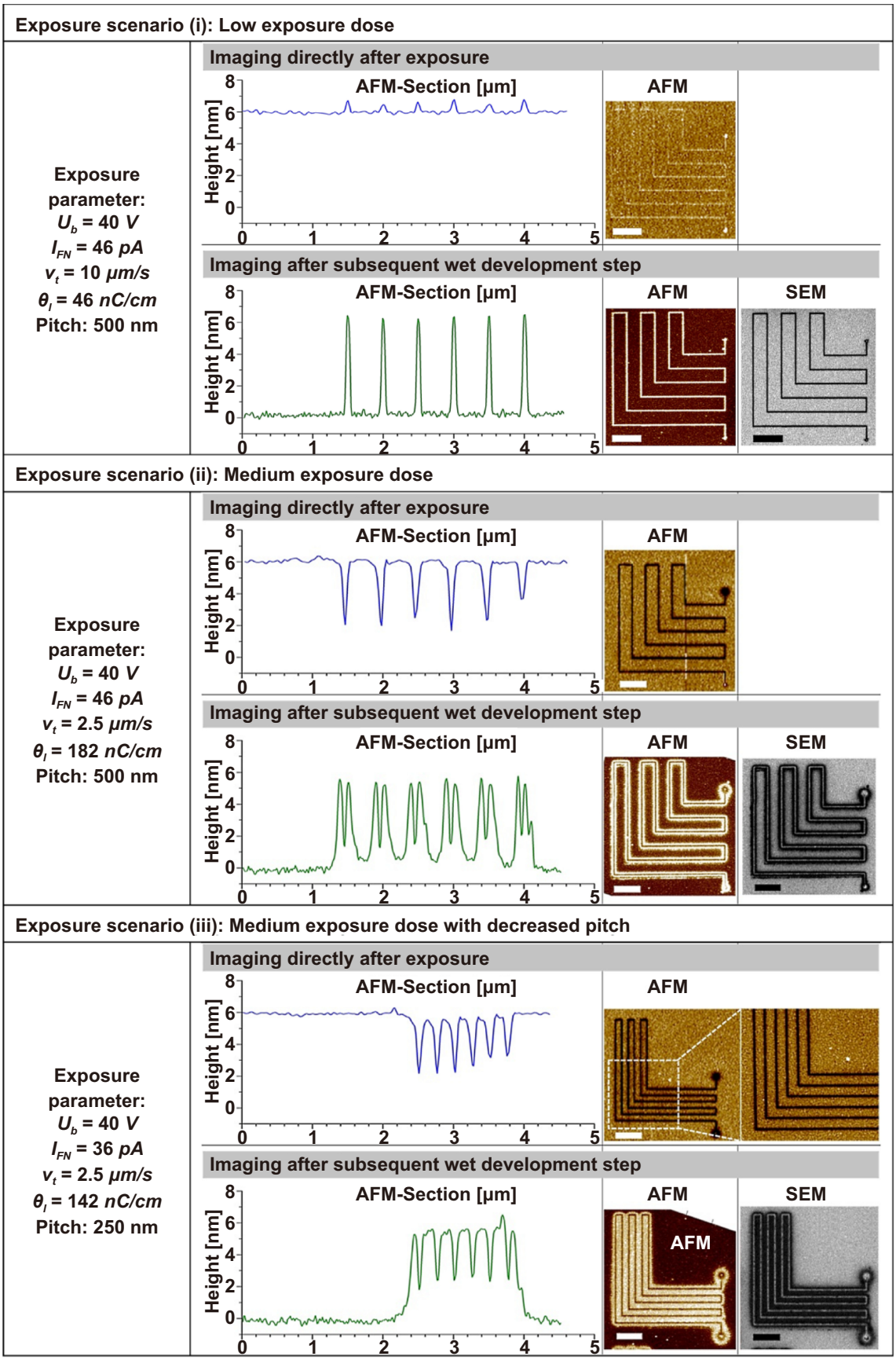

Figure 3. FE-SPL line patterning series showing the alteration of the lithographic interactions for different line dose and line pitch combinations. The trenches were measured after exposure corresponding to the directly ablated resist. The crosslinked resist, colored in green, was measured after a wet development step. Unmodified resist is colored in light blue. Scale bar size: 1 μm.

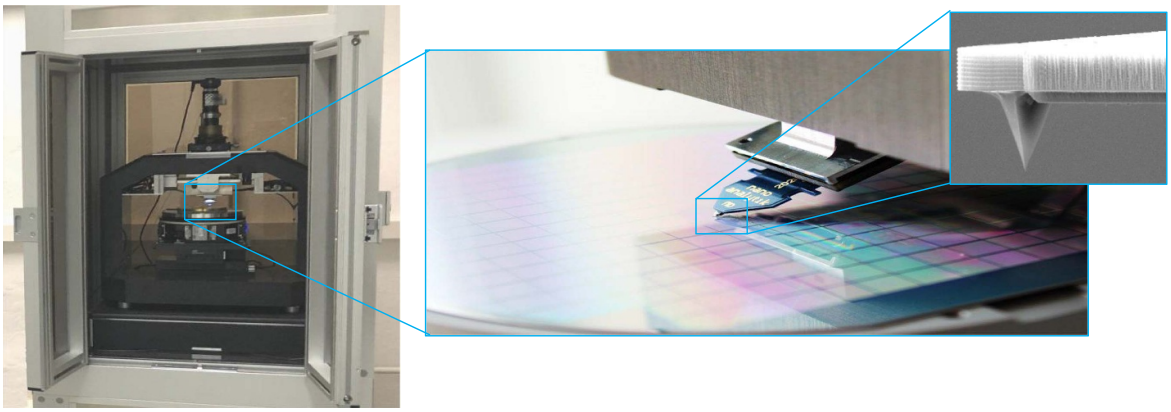

Figure 4. Scanning-probe type FE-SPL /AFM 150 mm- tool and zoomed view of the cantilever and the field emission tip over the 150 mm wafer sample (Courtesy nano analytik GmbH, Germany).

the nanofabrication, field emission scanning probe lithography was introduced and employment of robust silicon, diamond- or GaN-tips with sub-10 nm radius demonstrated [77].

In electron-exposure mode, the current between the tip and the sample is used for the closed-loop control, which directly reacts by adjusting the z-actuator voltages to maintain the desired current signal at the set-point due to variation in the tip-substrate distance. In the imaging mode, an active cantilever deflection signal is simultaneously monitored in order to prevent the tip from crashing and damaging the sample and the tip.

Two separate feedback loops were integrated in the FPGA control system from Nanoanalytik GmbH [64]. For the imaging mode of the system a standard AM (amplitude modulation)—AFM feedback loop was implemented. For the lithographic operation mode of the system a current based feedback loop was integrated, which maintains a constant current (cc: constant current mode) between tip and sample by respective modulations of the tip-sample spacing. The lithographic exposure dose, which is a function of the current set-point and velocity of the probe, was exactly controlled, adjusted, and kept constant for patterning at constant exposure requirements. Therefore, the measured current was converted into a respective voltage signal, amplified, filtered, digitalized, and fed into a PID based feedback loop control, which generated an output signal that controlled the Z-position of the probe. The custom-designed I-U converter and amplification stage had a switchable transfer function of 5 V nA^{-1} and 0.5 V nA^{-1}. For low dose operation the 5 V nA^{-1} option was chosen, characterized by an RMS noise of <100 fA. The lowest applicable exposure dose was approximately 1.9 fC in spot exposure and 2 nC cm^{-1} in line exposure, respectively. In the lithographic operation, the tip was virtually grounded through the IU converter unit, whereas the sample was biased using an external high-voltage, low-noise source. Dynamic switching between closed loop imaging and lithography mode allowed for sequential read/write cycle-based patterning schemes, discussed in more detail in [28]. For standard electron beam lithography exposure, a 30 kV Gaussian system (thermal Schottky emitter) was applied and operated at 10 keV beam energy and 0.21 nA electron beam current.

Ultra-thin (5–50 nm) calixarene resist films were prepared by a standard spin-coating process [59]. In particular, the calixarene derivate C-methylcalix[4]resorcinarene (CMC4R, $C_{32}H_{32}O_6$, molecular weight: 544.59 g mol^{-1}) was applied. Spin-coating solutions of CMC4R were prepared by dissolving the calixarene in methyl isobutyl ketone. The solution was filtered prior to spin-coating by using a Teflon syringe filter (0.2 μm). The resist thickness is adjustable by altering the concentration of the solution (e.g. a 5.7 mmol l^{-1} CMC4R solution results in a ~10 nm resist layer) [57–59]. The spin-coating process was performed at 2000 rpm for 3 s and 3000 rpm for 30 s. A prebake step was carried out at 90 °C for 3 min on a hot plate. The prepared amorphous resist films show uniform roughness properties in AFM imaging. Different prestructured sample types were used as substrates: (i) Si-surfaces covered with a conductive bottom layer (5 nm Cr followed by 15 nm Au) and (ii) moderately doped Si surfaces (p-Si, typ. 9–15 Ω cm, <100>). Due to the relatively large equivalent tip-sample resistivity the requirement concerning the conductivity layer below the resist is not as stringent. Moderately doped Si surfaces and even doped Si surfaces covered with thin oxide layers did not diminish the functionality of the current-feedback loop during patterning. The surface roughness of the films ranged between 0.25–0.35 nm when prepared on Si surfaces and between 0.4–0.7 nm on the Cr/Au bottom layer. Due to the increase of surface roughness induced by the metallic layers, the highest lithographic resolution was achieved on ultra-thin resist layers prepared on top of Si surfaces. The wet development step of the CMC4R resist film was carried out by a 10 s immersion in methyl isobutyl ketone (MIBK) solvent.

4. Mechanisms of exposure with low energy electrons

Quantitative changes to the exposure dose in FE-SPL leads to qualitative changes in the lithographic behavior of the calixarene molecular glass resist. The derivable patterning modes and tones are graphically summarized in figure 6. In general, the final lithographic outcome can be described by a

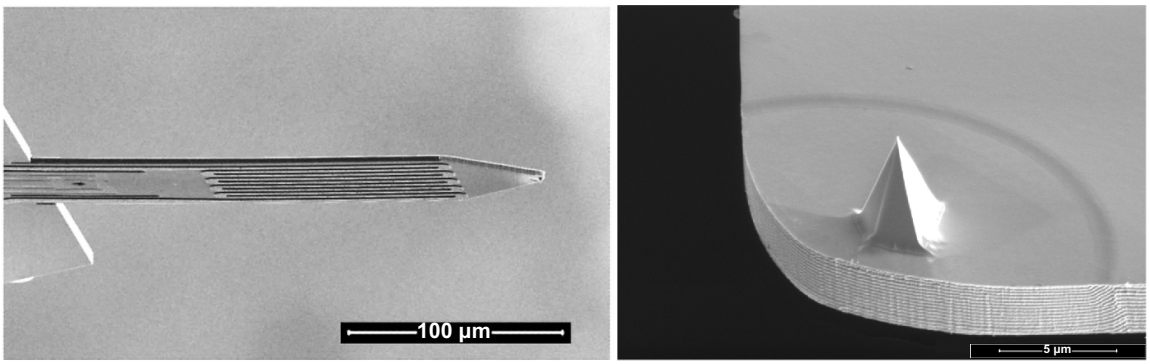

Figure 5. (a) SEM side view image of the probe with integrated piezoresistive read-out and thermomechanical actuation (active cantilever). A sharp 5.6 μm high silicon tip [58] (b) at the end of the cantilever ensures advanced AFM imaging and SPL capabilities. (a) Reprinted with permission from [58]. Copyright (2017), AIP Publishing LLC.

superposition of two distinct lithographic interactions: crosslinking and direct ablation of the resist material.

Thereby, crosslinking represents a material modification, while direct ablation is a material transformation from non-volatile to volatile parts, whereas the phenomenon of crosslinking of resist is in agreement with the negative tone behavior found in high-energy electron beam lithography [14, 47, 49]. The direct ablation of the resist was unexpected and contradicts the standard high-energy EBL, which was carried out in high vacuum conditions.

The experimental results for spot and line exposure characteristics are summarized in figures 7(a) and (b), respectively. It appears that both interactions were linked. For a explanation of this effect, we suggest the application of a simple Gaussian beam model, initially suggested by Wilder *et al* to describe the crosslinking interaction in low-energy exposure [34]. Simulations and experiments done by ourselves and others [33, 34] support using a Gaussian distribution to describe the electron exposure dose and related absorbed energy density. This also implies that low-energy electrons induce practically no backscattering during the crosslinking process. The dense line/space patterning experiments we carried gave no indications of the proximity effects observed in standard EBL. The width-dose dependency shows a logarithmic function which was observed for both spot (figure 7(a)) and line (figure 7(b) exposure modes). Returning to the self-alignment feature, the correlation between the crosslinked areas, which remains after wet development, is defined by the difference in thresholds and the related exposure doses. However, the model does not take into account a possible lateral diffusion of reactive species in resist.

In our setup, the lowest applicable exposure dose was limited to approximately 1.9 fC in the spot exposure mode and 2 nC cm^{-1} in line exposure mode. However, the threshold for the resist crosslinking reaction of calixarene falls below these values. Thus, the systems' hardware limitations prevents us from determining the gel and saturation dose as well as the contrast curve in FE-SPL, for both dot and line patterning. Nonetheless, a spot dose threshold for crosslinking of 1.7 fC was approximated. The smallest dots achieved in our actual setup were created by 1.9 fC, which corresponds to less than 1.2×10^4 electrons per single dot. The tip-sample convolution corrected diameter at FWHM of the corresponding dot was estimated at approximately 10 nm. An amount of approximately 10 electrons per single calixarene molecule (molecular size of approx. 0.75 nm) can be derived, which is a remarkably low value. In contrast, the high-energy EBL spot exposure tests carried out by Fujita *et al* had a minimum point exposure dose of 1×10^5 electrons/dot for calixarene at an acceleration voltage of 50 kV [14]. Here, minimum pixel sizes of ≈12 nm were achieved. Thus, the spot exposure dose of EBL was more than 10-times larger compared to the FE-SPL exposure, which was carried out at 30 V bias voltage. The required FE-SPL spot dose is even lower than that for the high sensitive positive tone PMMA polymeric resist (5×10^4 electrons/dot for minimum dot sizes of ≈20 nm [14]).

Direct ablation is characterized by a significantly higher threshold compared to the crosslinking of the resist (figure 7(b)). In the particular example, a ratio of approximately 17 was measured. This is shown in figure 7(b) (semi-logarithmic plot), for example curve #2 represents twice the exposure dose of curve #1.

For example, curve #1 in figure 7(b) exceeds the crosslinking threshold, whereas curve #2 shows that the threshold for ablation was not reached. In this case only a crosslinking interaction is induced (ablation not triggered). Its lateral confinement is defined by the intersections of the dose distribution function with the particular fixed threshold value. For example, the threshold value of curve #1 ranges from −74 to +74 a.u. The width of the crosslinking reaction extends with increasing exposure dose (e.g. two and three times the absolute dose of curve #1 depicted by curve #2). Increasing the second threshold value associated with the direct ablation process, is exceeded.

The electric potential difference between the tip and sample generates a strong electric field (figure 8(a)), which induces a spatially localized field emission current. The emitted current can be described by Fowler–Nordheim emission [60, 61].

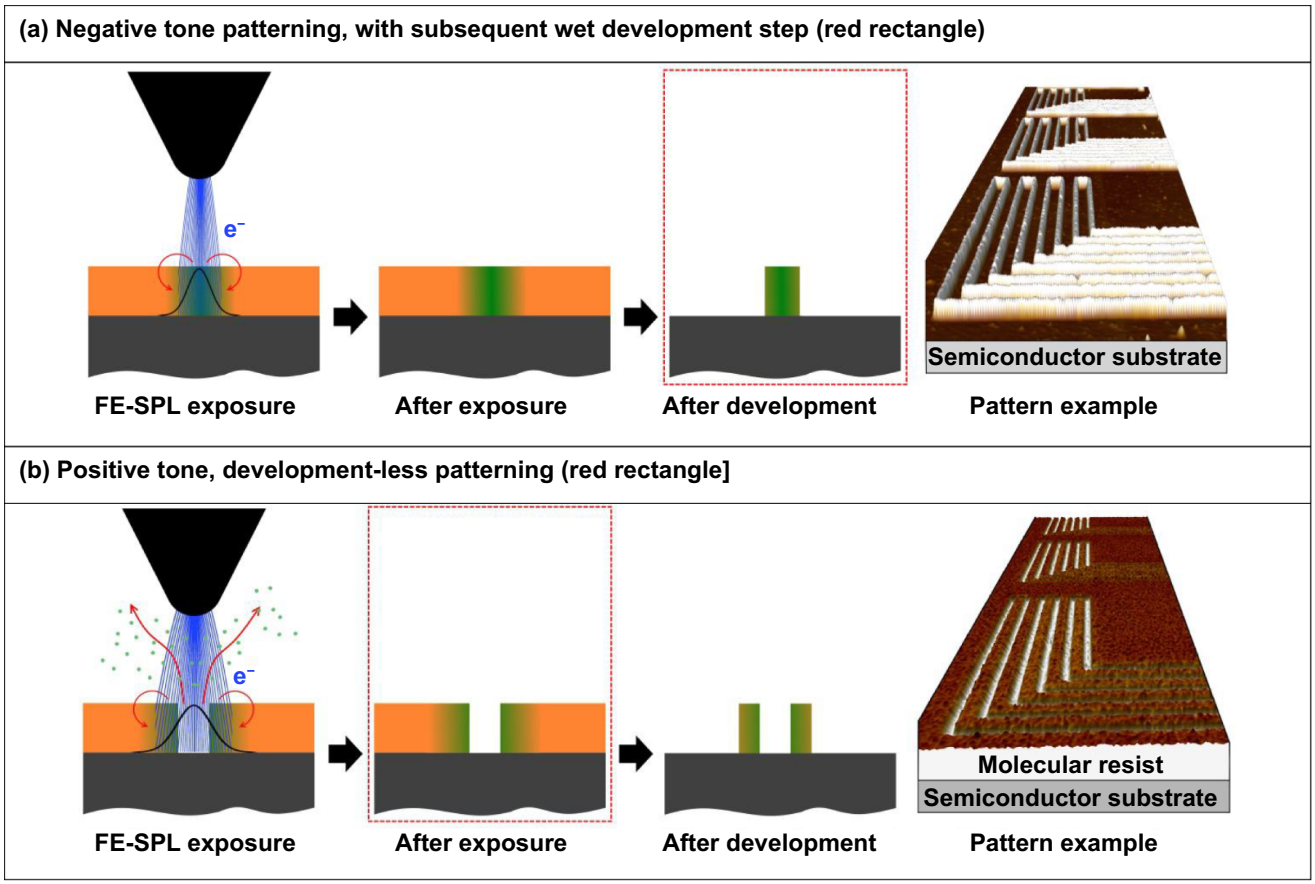

Figure 6. Schematic summary of the patterning modes: (a) negative tone patterning including wet development and (b) positive tone patterning without development. In order to enhance the resolution of the FE-SPL patterning, the double patterning technique could be introduced using development. The corresponding AFM topographic images on the right side of the schematics were acquired after the process step and denoted by a red-rectangle.

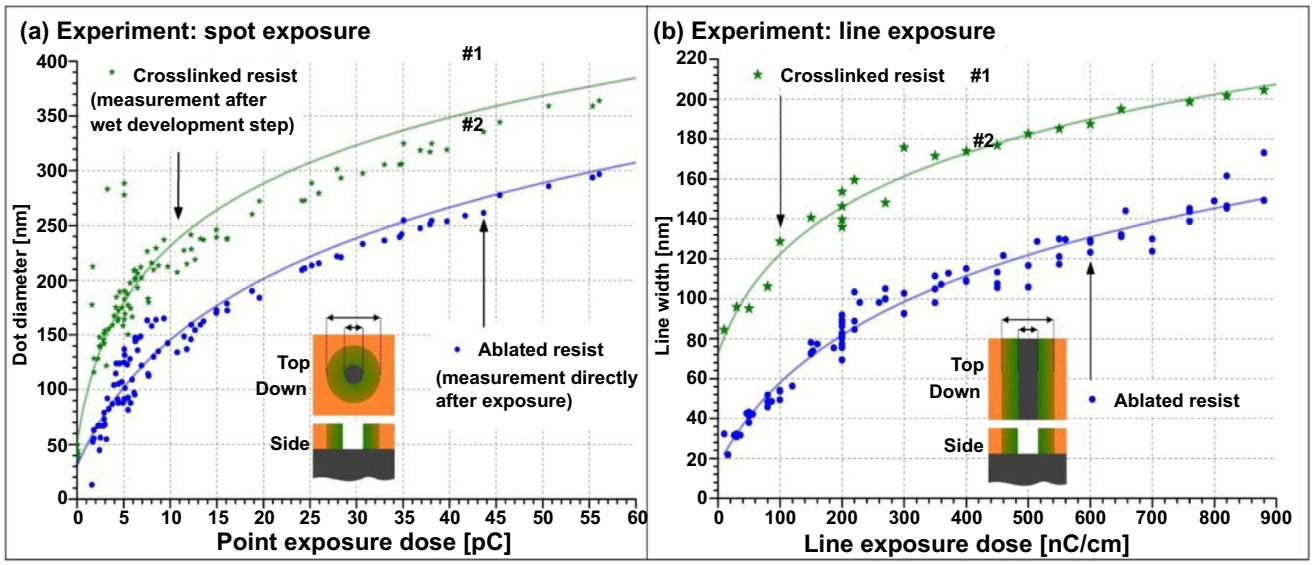

Figure 7. Lithographic spatial confinement and experimentally derived model. Lateral extension of the crosslinked (green stars) and the ablated resist (blue dots) as a function of the electron exposure dose. The experimental results for both cases spot (a) and line exposure (b) are shown, respectively.

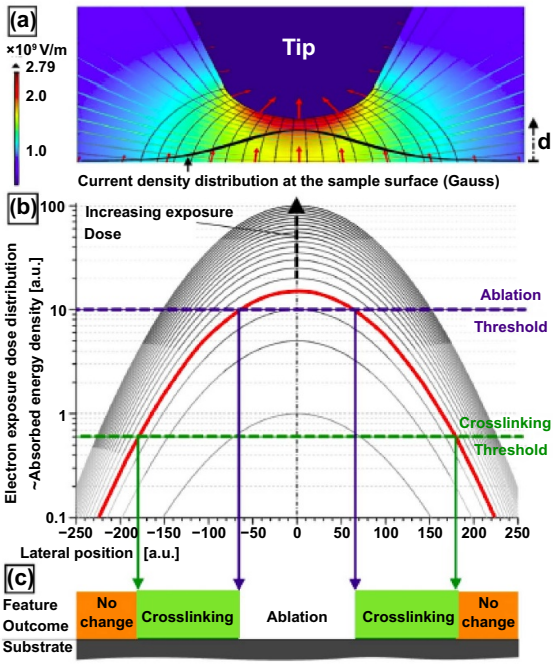

Figure 8. Qualitative description of the lithographic spatial confinement by a Gaussian beam model with two separate resist related exposure threshold values. In this particular example, the exposure dose (~absorbed energy) threshold for resist ablation was approximately 17-times higher than the crosslinking threshold. (a) Electric field and current density distribution simulation of the tip-sample system (spacing between tip and resist d = 15 nm; bias voltage = 40 V; resist: 20 nm and $\varepsilon_r = 3.7$; $r_{tip} = 15$ nm); (d) labeling of the lithographic interaction based on the lateral position in reference to the center of the incident Gaussian beam; (b) electron exposure dose distribution, which is a measure for the absorbed energy density in the resist, is plotted as function of lateral position. Thereby, the zero lateral position represents the center of the incident low-energy electron beam emitted from the tip.

A Gaussian distribution provides an adequate initial approximation of the local current density distribution at the tip-resist interface the electron exposure dose distribution, and the related absorbed energy density distribution. Under identical exposure conditions and equal electron energy, one can express the lateral distribution by a summation of Gaussians.

As summarized in figure 8(b), the model is modified by the introduction of different electron exposure dose threshold values, which are associated with the two different lithographic effects: crosslinking and ablation.

In terms of vector-based line patterning, an even higher difference between EBL and FE-SPL exposure dose was determined. Here, a line exposure dose test on the same sample (≈24 nm thick calixarene resist film) was performed using EBL at 10 keV and FE-SPL at 40 eV, respectively. The corresponding results are summarized in figure 9 by plotting the normalized resist thickness vs. line exposure dose. In the case of crosslinking, valid for high energy EBL (green stars) and low dose exposure FE-SPL (green dots), the remaining normalized resist thickness after wet development (WD) is measured (left vertical axis) as function of line dose.

Significant differences in the crosslinking thresholds between FE-SPL and EBL were observed. For 10 keV EBL, a critical gel dose of ≈92 nC cm^{-1}, was derived. A saturation dose, which indicates the sensitivity of the resist, was determined as 164 nC cm^{-1}. The resist contrast for EBL was ≈3.9, represented as a green line in figure 9. This is in agreement with published reference data [28]. When FE-SPL was already at the lowest applicable exposure dose of 2 nC cm^{-1} (hardware limited), a complete crosslinking process through the entire resist film thickness was induced. The crosslinked resist height was measured at low-exposure doses ⩽ 10 nC cm^{-1} after the wet development and plotted in figure 9 by green dots. The complete resist layer was rendered insoluble by the low-energy exposure in ambient conditions. No changes were observed in the resist height. We could not determine the linked threshold doses or the resist contrast curve because the onset of the crosslinking process occurred below the measurement limit of our FE-SPL system. This means that even the lowest applicable exposure doses can trigger a crosslinking process, which leads to a solubility change. Thus, we can only reason that the saturation dose range falls below the 2 nC cm^{-1} line dose. Applying low-energy FE-SPL in ambient conditions was over 80-times more sensitive than EBL.

When moving towards higher exposure doses in FE-SPL, the onset of a centered direct resist removal is reached. In figure 9, this occurs when the ablation threshold of ≈21 nC cm^{-1} is exceeded. Thus, at exposure doses larger than 10 nC cm^{-1} for FE-SPL, the normalized ablation depth, which was measured directly after exposure, is plotted as function of line dose (figure 9, *blue dots related to the right-hand side vertical axis*). Thereby, the threshold line dose for removal in FE-SPL is located in the gel exposure dose range of standard EBL, at which the crosslinking process is initiated. Conversely, an increase in the exposure dose exceeding the saturation dose does not change of the pattern characteristics of EBL.

The graph in figure 10 is a lin-log plot (Y-axis → lin; X-axis → log). This plot is commonly used in standard electron beam lithography to determine the sensitivity and gel dose of the resist. However, the graph the EBL (green) data shows a straight line in lin-log plot, whereas the FE-SPL data does not correspond with the EBL behavior. The linear dependency of ablation depth on exposure dose can be seen in figure 10, (i) a lin-lin plot type.

In the example shown in figure 9, a slope of approximately 0.029 nm/(nC cm^{-1}) is determined. This suggests that an increase in line exposure dose is associated with an increased width of directly ablated trench. This effect is experimentally illustrated in figures 7(a) and (b) and by model in figures 5(a) and (b). Resist thicknesses <10 nm are mandatory to achieve the highest resolution at full clearance of thin resist films.

The spacing between the tip and sample as a function of the applied bias voltage is plotted in figure 10. a silicon layer was applied on the to act a reference level for the height measurements. A linear behavior between applied bias voltage and tip-sample spacing was observed similar to behavior predicted by the Fowler–Nordheim field emission theory. A slope of ~0.7 nm V^{-1} was derived. Raising the bias voltage increases the tip-sample spacing, which broadens the electron beam. Thereby, the applicable bias range is defined by the

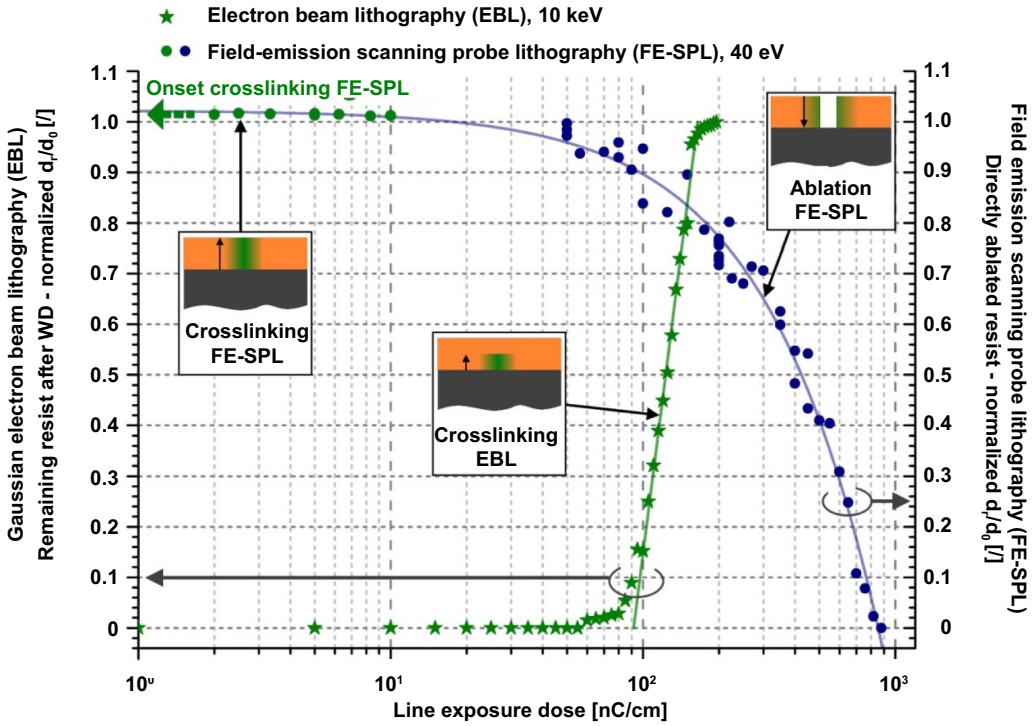

Figure 9. Comparison of the exposure characteristics of calixarene molecular glass resist at 10 keV electron beam lithography (green stars: crosslinking → negative tone) and 40 eV field emission scanning probe lithography (green dots: centered crosslinking → negative tone; blue dots: centered ablation → positive tone).

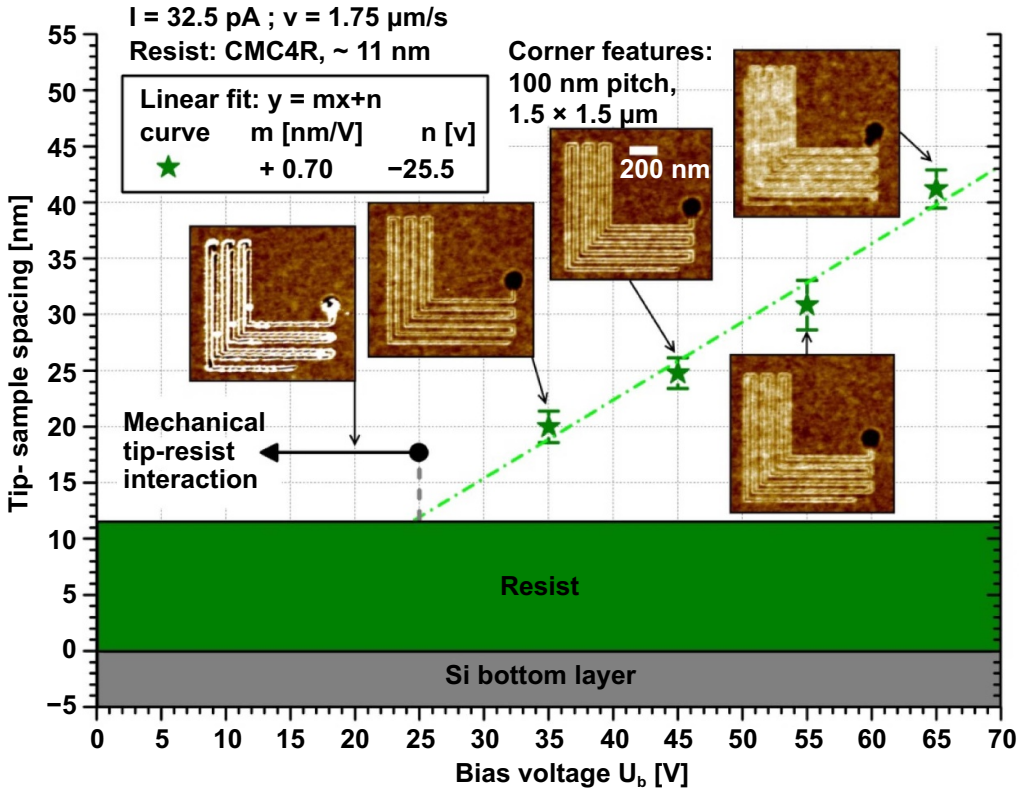

Figure 10. Tip-sample spacing as function of applied bias voltage.

mechanical interaction/scratching regime that occurs at low-bias voltages. The extremely broadening/multi-spot emission occurs at high bias voltages. Both extremes are depicted in the AFM topography insets of patterned L-corner features.

Figure 11 provides a plot of the dependencies of the direct ablation lithographic reaction as function of applied exposure dose: (i) represents the ablation depth as a function of line dose. The ablation-dose dependency is described by a linear function. The line width versus exposure dose dependency, summarized in (ii), is adequately described by a logarithmic function. The composition of the line dose characteristics of the current set-point (linear scale) and tip velocity (log-scale) is shown in figures 11(iii) and (iv). The line dose increases within the bottom plant of the velocity-set-point towards higher set-points and lower velocities. The corresponding exposure dose test, from which the measurement data was extracted, was written at a bias voltage of 35 V into a ~18 nm thick 4m1ac68 resist layer.

5. Influence of the environment

Regarding low-energy electron exposure for crosslinking of polymeric resists, Kragler reported that the surface degradation of the resist films was enhanced during days with increased relative ambient humidity [62, 76]. Thus, all results point towards an amplification of the degradation with increasing OH-group content. OH is present not only in the gaseous environment but also as a thin layer on the resist-air interface. It is also stored within the resist itself (*depending on its hygroscopic properties*). So far, OH in the form of water works as additional source of reactive species. Initial reactions within the water layer itself are likely since the MFP and the IMFP of the applied low-energy electrons range below the typical water layer thicknesses at ambient conditions [52]. The generation of highly reactive hydroxyl radicals (OH· is a powerful oxidizing agent) and ions could be seen as a chemical enhancement/amplification source of lithographic reactions. According to the work of Kondo *et al* [78], chemical reaction paths with lower activation energies are favored in ambient conditions, which are not accessible in vacuum conditions. In this context, we suggest that oxidative degradation of the resist material from non-volatile into volatile compounds was responsible for the direct ablation of the resist material in the exposure center.

Our insights gained in ambient low-energy FE-SPL support the assumption that the hydroxyl (–OH) functional groups of the calixarene molecules play a significant role in the crosslinking process. Using a molecular glass resist derivate without functional groups, no crosslinking could be achieved. Thus, the experimental evidence supports a model in which crosslinking is a resist-specific process rather than a generic process. One can further deduce from Fujita's [28] heuristic model, that low-energy electron exposure is more efficient. Based on his explanation of the exposure process, energy transfers to specific narrow energy bands of the resist molecules. Thereby, the target bond excitation efficiency is a function of the energy lost from the involved electrons. Only energy losses in the order of several eV can excite the target bond reaction. Thus, in standard EBL, the triggered secondary electrons are responsible for the lithographic processes. Here, the calculated Vries exposure reaction cross sections are located in this energetic range of 8–12 eV for relevant binding strengths. The low-energy electrons in FE-SPL are close to those energetic bands, which could be one explanation for the increased exposure efficiency.

In spot exposure at standard environmental conditions, a threshold dose of 1.2 pC for direct ablation was derived, which corresponds to approximately 7.5×10^6 electrons/dot. At a spot dose of 2 pC (which is the lowest measured value above the estimated threshold), an average of 350–1000 electrons per resist molecule are required to achieve a full degradation into volatile products. This value is about 50–150 times larger than the threshold required for crosslinking.

So far, studies comparing low-energy FE-SPL and standard high-energy EBL have shown a reduced sensitivity in FE-SPL for highly sensitive EBL resist systems.

The exact mechanisms of crosslinking in FE-SPL are still not fully understood and remain open for discussion. For practical application, łow-energy electrons (<100 eV) can overcome the poor sensitivities of molecular glass resists while enhancing their ultra-high-resolution capabilities. Furthermore, exposure by low-energy electrons effectively suppresses backscattering. Thus, practically no proximity effects are present. The ablation process seems to be a residual free process since no redeposited material can be found on either the tip surface or aside from the pattern in the resist. This is shown in [79] by large field removal patterns. In the ablation regime, previously explained by a simple two-threshold Gaussian dose distribution model, a superposition of both lithographic interactions—crosslinking and ablation—is taking place.

Due to the small molecular size of calixarene, the line edge (LER) and line width roughness (LWR) are improved. Keeping the variation in electron exposure intensity in the range of 5%, 1 sigma LER less than 2 nm was achieved (figure 12).

In the case of the molecular glass resist calixarene, the mechanism of self-development (direct removal of resist) seems to be associated with an initial crosslinking of the resist. This impression is given by the fact that crosslinking has a lower threshold exposure dose compared to ablation. However, we have experimental evidence that suggests an initial crosslinking process is not a stringent requirement for ablation. It is also possible to induce a direct ablation reaction in other tested resists containing aromatic units, connected via C–C bonds, but without any functional chemical groups or tertiary C-atoms. Conversely, crosslinking of the resist was not measurable prior to neither ablation nor aside from the features. The ablation threshold doses for those particular molecules are located in the same range of calixarene resist. Therefore, one can derive that the functional groups in the calixarene (O–H, -oxymethyl, etc) resist are responsible for effective crosslinking, but they are not relevant for ablation. We observed the ablative effect in polymeric resists, such as PMMA, PS, and PHS. The response of different polymeric resist types (e.g. PMMA, PS, and PHS) were investigated and reported [80]. As experimentally revealed, all organic resist materials showed

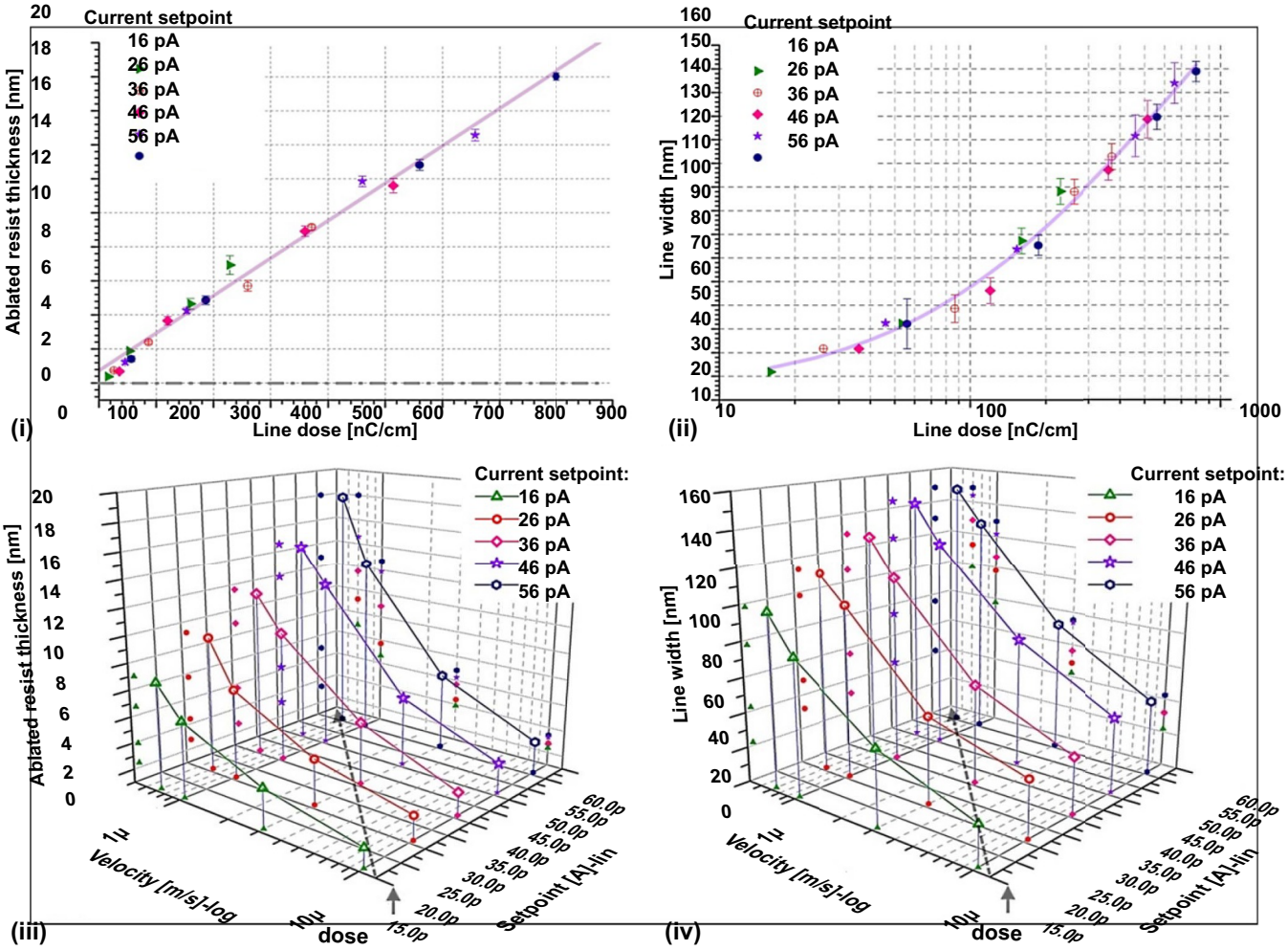

Figure 11. Dependencies of the direct ablation lithographic reaction (positive, development-less tone) as function of applied exposure dose in vector-based line patterning.

the general oxidative based ablation behavior. The only exception found so far is the fluorinated (F-terminated) resist which showed a sole crosslinking process resulting in a pure negative tone behavior. Thereby, the formed fluorinated network inhibited further oxidative degradation within the evaluated exposure dose range. Consequently, no ablative reactions were observed. In contrast, molecular resists that do not have functional groups still show a direct ablation. However, sufficient crosslinking reaction was not observed when OH- and F-groups were absent. In conclusion, the hydroxyl (OH-) groups of the calixarene molecule enable an effective crosslinking process at low doses, but still facilitate a direct ablation reaction at increased dose levels. A superposition of crosslinking and direct ablation was only observed in calixarene MG resists (see sections 1 and 4). This unique combination of crosslinking and ablation led to the formation of self-aligned double line (in the case of vector based line exposure) and doughnut (in the case of spot exposure) features. Furthermore, calixarene resist alone allows for tone-switching from negative to positive tone with increasing dose. In conclusion, the hydroxyl groups in calixarene are responsible for an effective crosslinking process, whereby these groups are not necessarily required for direct ablation. Here, the ablative processing of resists is still enabled when having only pure aromatic systems without any functionalization.

In contrast, polymeric resists show limited resolution capability compared to molecular based resists (e.g. calixarene). We propose that the effects described by Lyuksyutov *et al* [81] in terms of electrostatic nanolithography are attributed to the oxidative degradation process into volatile compounds we observed. Thus, the direct ablation in ambient conditions, triggered by the field emitted low-energy electrons is a resist-unspecific effect rather than a specific effect.

Thermal effects can be excluded because FE-SPL works in a low-current operation range of less than 100 pA . This is substantiated by calculations carried out by Perkins *et al* [33]. Due to the chemical reaction pathways, the environmental conditions as a source of reactive chemical groups have significant influence on the lithographic result.

An increased number of oxidative OH species, (e.g. at enhanced relative humidity) led to an enhanced ablation.

The threshold for ablation depends on the water content of the exposure environment. This includes the influence of the

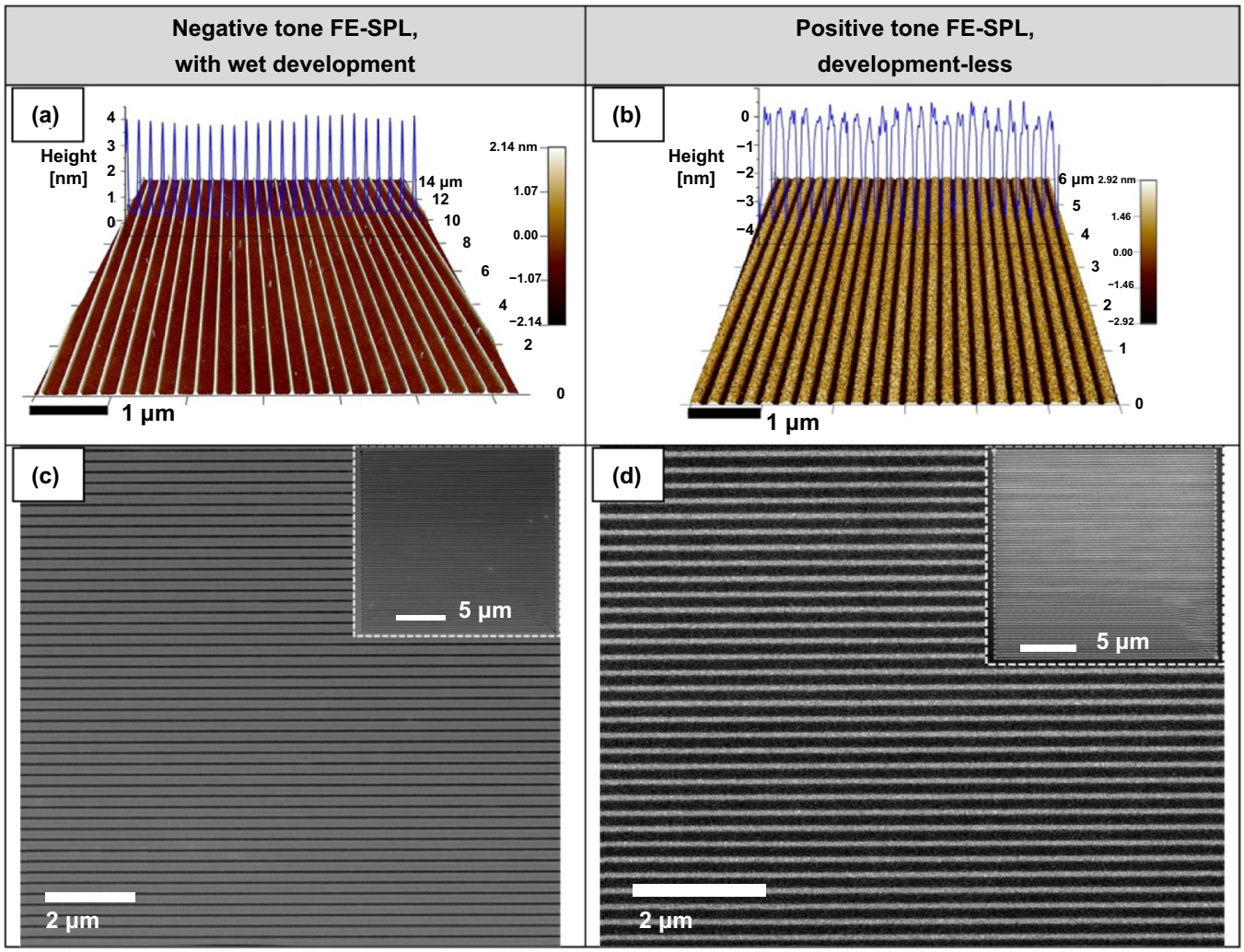

Figure 12. The 3D AFM topographic image and the corresponding section graph are not convolution-corrected. The measurement depth is tip-limited ($r_{tip} \leqslant 10$ nm specified). (b) Large-scale line patterning demonstration of FE-SPL in both lithographic tones, imaged by AFM (b), (c) and SEM (d), (e). The exposure doses were chosen respectively: low dose (25 nC cm^{-1}) for negative tone and high dose (142 nC cm^{-1}) for positive tone development-less patterning (bias voltage in both cases 35 V).

relative humidity as well as the water adsorbed at the resist-air interface (i.e. water layer) and the water absorbed within the resist film itself (depends on hygroscopic properties of the resist). As a result, the threshold for ablation can be modulated by the probe-surrounding environment. The environmental modulation of the water content is quantitatively described by a shift in the ablation threshold. Thereby, only the threshold value is altered but not the removal rate itself (figure 13). An increase in the gaseous water content induces a shift of the threshold towards lower exposure doses. Thus, treatment with moisturized process gases promotes direct ablation; whereas treatment with dry inert gases suppresses the ablation, yielding a sole crosslinking process. This behavior can be clearly seen in figure 14 Since the absorbed and adsorbed water within and on top of the resist influences the lithographic process, a hysteresis effect between gaseous treatment and lithographic reaction exists. This means that the ablation threshold is not restored immediately after returning to the initial conditions. Instead, some intermediate state is present. This is known as the 'background and history' of the lithographic sample matter. Since the lithographic process is strongly influenced by the humidity level, it is crucial to maintain a stable exposure environment. The treatment history of the sample must be controlled in order to achieve reproducible results. As previously described, H_2O molecules chemical enhance the direct ablation reaction. Thus, the findings support that the direct resist removal (ablation) mechanism is based on oxidative degradation of the resist.

Additionally, we investigated the same exposure setup under environmental and high vacuum conditions. We employed the AFMinSEM instrument (figure 15) from nano analytik GmbH, which can characterize surface topography, mechanical properties, electrical properties, and magnetic properties [64, 79, 81–89].

Figure 16 shows a comparison of FE-SPL exposure realized under ambient conditions and high vacuum with the same exposure dose and energy. The patterning conditions during the experiments were tip bias voltage of—40 V, field-emission

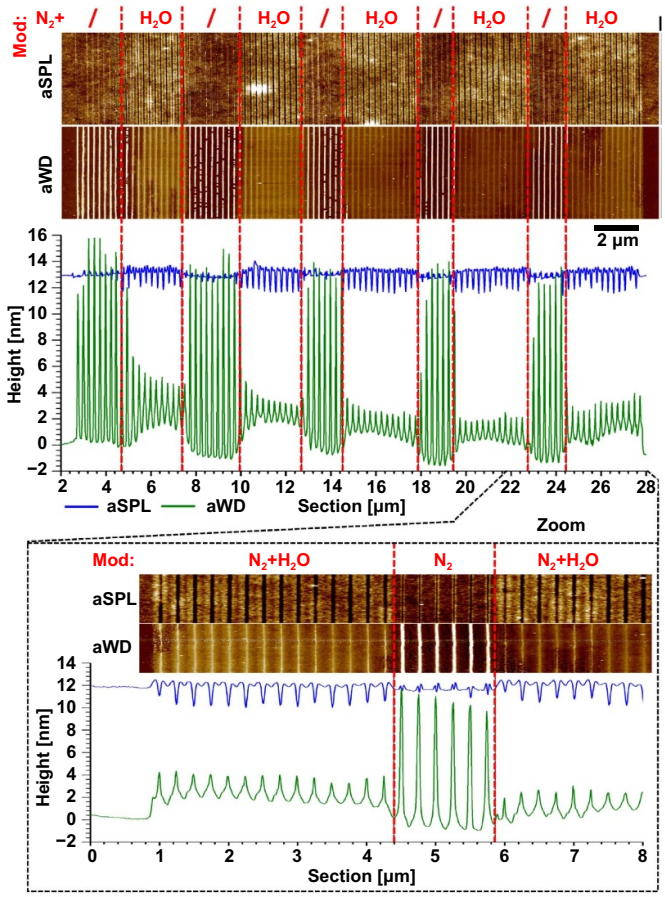

Figure 13. Investigation of the impact of dynamic changes of the gaseous water content within an individual pattern on the lithographic outcome. During patterning of large-scale meander ($12 \times 25\ \mu m^2$, 250 nm pitch, total length of 2.05 mm) by FE-SPL (Ub = 35 V, _L = 150 nC cm^{-1}) the probe-surrounding environment was changed by alternating between dry N2 and moisturized N_2 ($N_2 + H_2O$) processing gases. The corresponding sections of a meander, which were exposed at a constant environment, are labeled accordingly. AFM imaging was carried out directly after exposure (aSPL) and after a subsequent wet development step (aWD). For the section plots an average of over 300 single lines were applied. In the lower part of the image, a zoom-in is provided showing the last 7 μm of the meander pattern (Sample: 12 nm thick 4m1ac68 resist, spin-coated on top of a pristine Si chip; probe: electrochemically etched tungsten wire (rtip: 16 nm)). Scale bar: 2 μm.

current of 15 pA, and tip velocity of 0.2 μm s^{-1}, resulting in a line dose of 750 nC cm^{-1}. A high stiffness cantilever with a resonance frequency of 100 kHz was used (spring constant 90 N m^{-1}). Figure 16 shows a positive tone exposure at ambient conditions. The role of OH groups is evident [63]. Exposures in a vacuum induces negative tone behavior, which requires a wet development step.

One of the most critical issues concerns the line width variation during long exposure periods. Figure 17 shows (a) SEM and (b) AFM images of donut-shaped resist rings created in a 6 nm thick calixarene resist. The images are characterized by inner and outer diameters of ≈10 nm and ≈30 nm, respectively. The smallest inner diameters created by the direct ablation effect (e.g. development-less, positive-tone) were smaller than 7 nm. Figure 17(c) shows an exposure test of 1.4 mm long features exposed without interrupting the exposure process. High-resolution and high-selectivity direct pattern transfer was demonstrated using 10 nm calixarene resist [86]. Its practical applicability was demonstrated by realizing room-temperature single electron transistors [87–91].

6. Conclusion

In this article, we summarized our current work contributing to a novel lithographic technology targeting sub-5 nm manufacturing of nanoscale devices. Combining a scanning nano-tip as an emitter of low-energy electrons with a molecular 'glass' resist provides unique lithographic capabilities. Utilizing low electron energy, effectively circumvented proximity effects, enhanced the sensitivity in crosslinking, and identified novel routes of direct ablation at the nano-scale.

The OH-groups were identified as the main facilitators within the oxidative resist degradation process, leading to a positive tone. As a result, volatile compounds were formed which, enabled self-developing pattern formation. Due to the superposition of crosslinking and ablation reactions, a self-aligned double line patterning was achieved (figure 18). The self-aligned double line patterning and its feature size was limited by the threshold Gaussian distribution. Furthermore, novel methods towards sub-5 nm patterning by using tone switching and mix-and-match methods [88] were demonstrated. For direct low-energy electron exposure, a Fowler–Nordheim field emission from a proximal probe tip was utilized. Dedicated Scanning Probe Lithography tools by Nanoanalytik GmbH, Germany have been developed.

In particular, the FE-SPL process using low-energy electrons in ambient conditions is at least 10-times more effective for dots and about 80-times more effective for lines compared to high-energy electron exposure. The radiation process in ambient conditions by low-energy electrons enables novel reaction paths, which are not accessible via standard high-energy electron beam lithography in UHV. This is manifested by two lithographic relevant phenomena: sensitivity enhancement in the crosslinking process and direct ablation of calixarene molecular glass resist.

The application of active scanning probes enables closed-loop patterning. By using the direct AFM-based imaging capability, one can directly inspect the patterned features. Imaging and lithographic cycles were applied in sequence, which means that every single feature was aligned separately with the highest precision and inspected directly after patterning. The direct measurement and inspection capability of the closed-loop lithography principle includes an integrated overlay and stitching routine, resulting in precision capabilities similar to those of active-cantilever imaging and electron-exposure. In addition, the read-back functionality tip-induced differences in the lithographic outcome can be

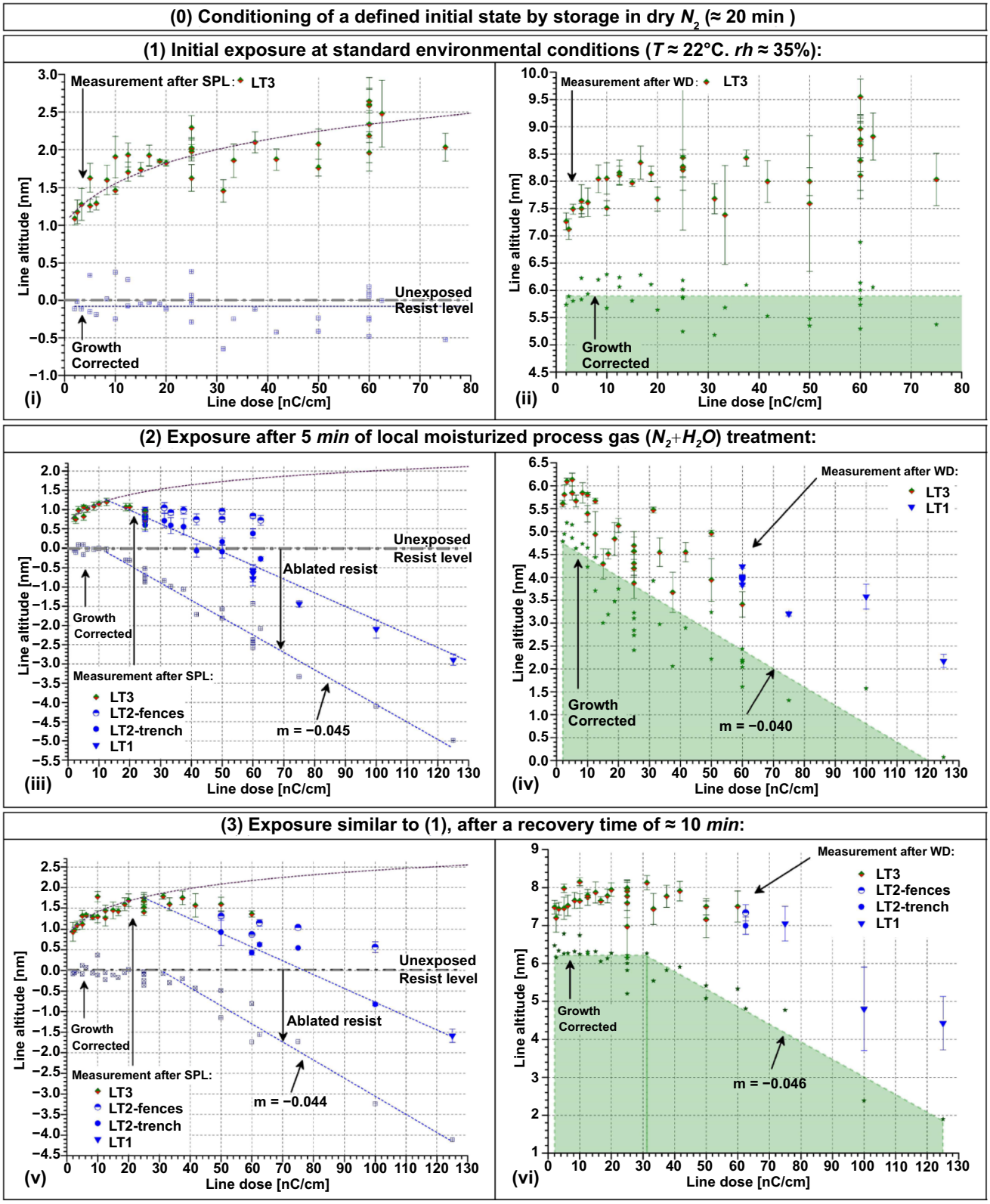

Figure 14. Tracing of the ablation threshold shift, caused by changes of the gaseous water content within the exposure environment. For this purpose an identical exposure dose test (Ub = 30 V) was repeated after distinct environmental modification steps (the same probe was used to exclude tip-induced effects), summarized by (1)–(3). Before the initial FE-SPL exposure (1) the sample was stored _ 20 min in a dry nitrogen atmosphere to have a defined initial state (0). In order to determine the ablation threshold, the line altitude was measured directly after exposure (i), (iii), (v) and after the wet development step (ii), (iv), (vi). (Sample: 5–6 nm thick cmc4r resist layer, PVD-coated on top of a Si chip).

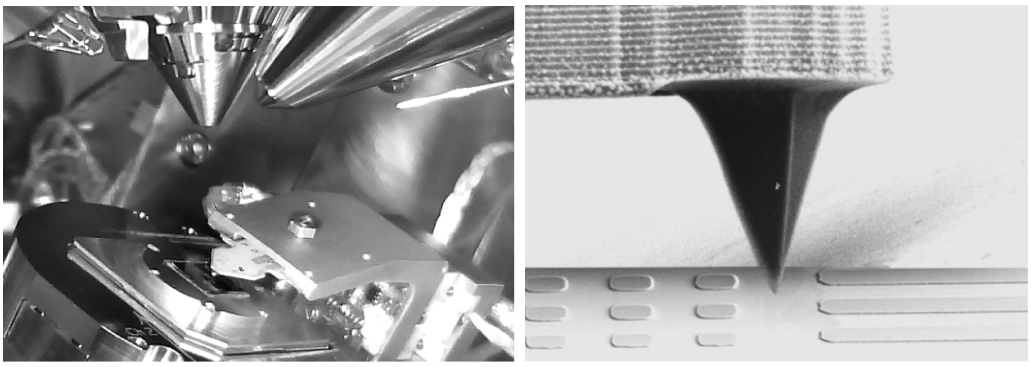

Figure 15. (a) AFM mounted on an SEM specimen stage. (top) AFMinSEM allows tilt angles from $+60^\circ$ to -10° providing imaging of the tip with the SEM during AFM operation due to unique arrangement of the general setup of the scanner and active 'plug and image' cantilever. (b) The optimal working distance (4 mm) of the SEM for simultaneous operation of both instruments and precise navigation of the 5.6 μm high AFM-tip to area of interest.

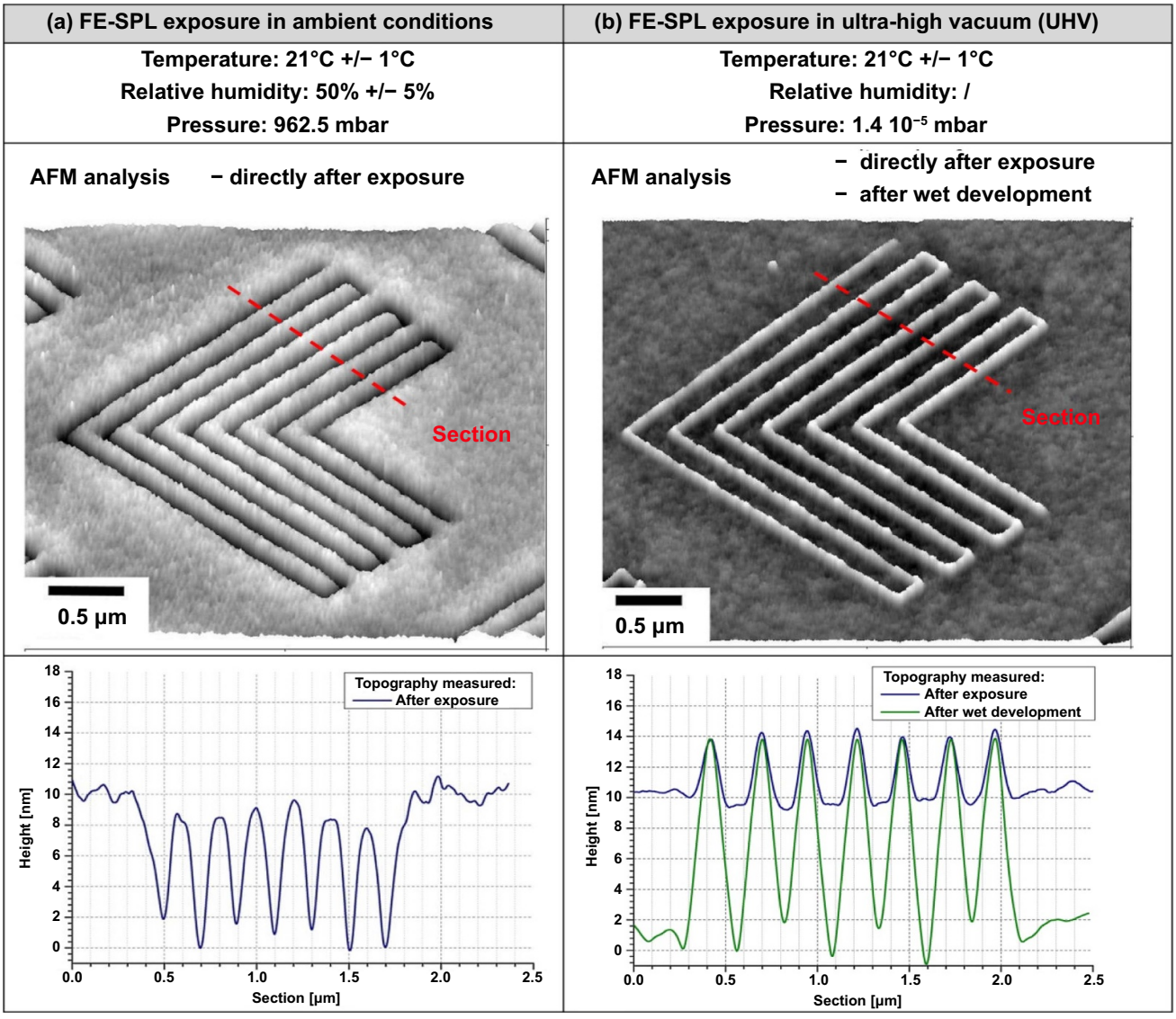

Figure 16. FE-SPL comparison exposure provided in ambient atmosphere (962.5 mbar) and vacuum (1.4 10^{-5} mbar) conditions. The exposure conditions were identical: line dose of 750 nC cm^{-1} and -40 V tip bias. Figure 9(a) shows a positive tone behavior where the resist is delayered during the exposure and figure 9(b) shows a negative tone (sample was wet developed).

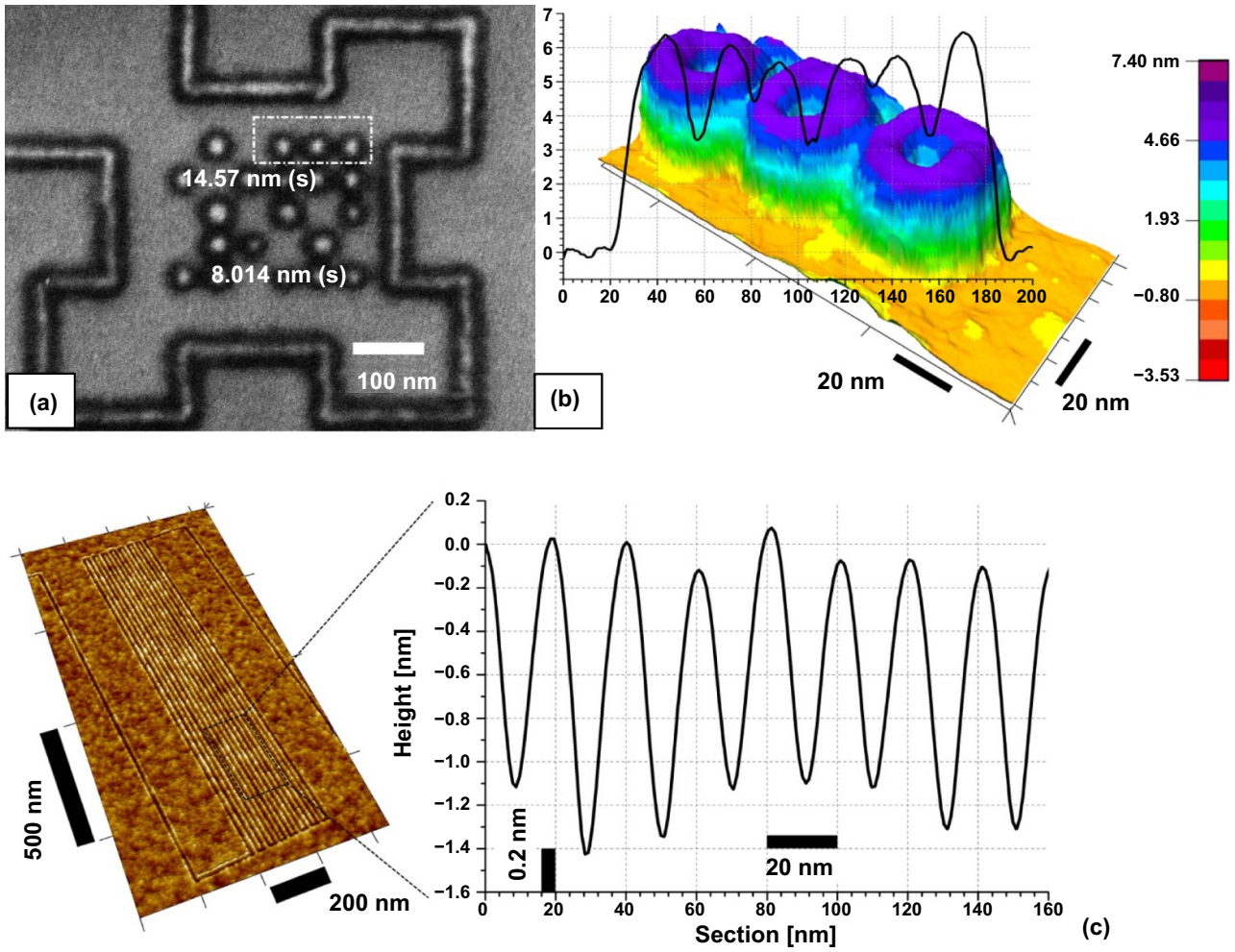

Figure 17. Donut-like features formed by a superimposed centered ablation of resist with surrounding crosslinking, measured after a wet development step (see figure 4). The spot exposure test array was imaged by SEM (a) and AFM (b). The donut-features were induced by a single spot exposure FE-SPL process (AFM topographic image and section graphs were not tip-convolution corrected). (c) AFM image showing a fragment of test 1.4 mm long features exposed without interrupting of the exposure process.

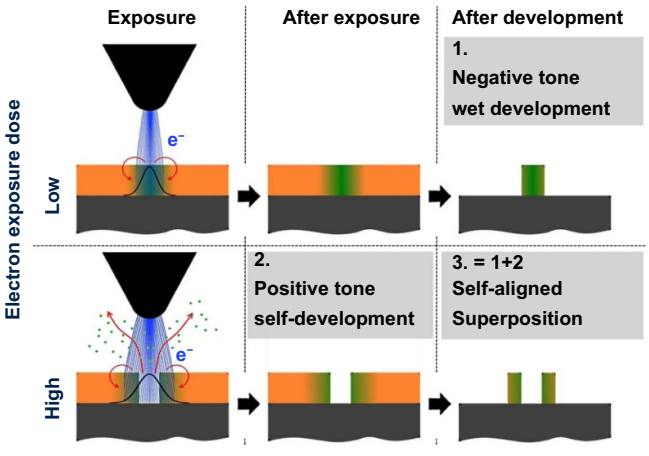

Figure 18. Principle of FE-SPL exposure-dose dependent lithography tones.

adaptively corrected. Thereby, the application of active cantilever probes, which integrates thermomechanical actuation, piezoresistive read-out and high aspect ratio, and sharp-tips, results in compact and ease-of-use nano-lithography systems [57–59, 79, 82–89, 92].

Like other serial lithographic methods that obey Tennant's law, such as EBL [12, 90], the FE-SPL is a serial process (imaging and patterning) and the main limiter of scanning probe technology throughput capability. Herein, the challenge affecting all serial lithographic technologies comprises the marriage of downscaling of device-relevant feature sizes towards single-nanometer resolution while simultaneously increasing throughput capability. With this in mind, the application of mix-and-match lithographic approaches that combines a high-resolution method with a higher throughput method for large scale patterning constitutes one of the most promising paths to break the resolution-throughput trade-off. We demonstrated a complementary mix-and-match lithography combining standard electron beam lithography with a closed-loop FE-SPL method for proof-of-concept [61]. In addition, using active cantilever arrays enables scalability, further enhancing the throughput capability [91].

Scanning probe lithography (SPL) has demonstrated its effectiveness in producing high-resolution structures (<10 nm) for research in nano-electronics, photonics, plasmonics, and magnetism. Beyond that, sub-5 nm alignment accuracy is given. SPL also shows great potential for forming 3D structures at comparable scales [88, 89, 92].

While at high-resolution, SPL has a writing speed comparable with that of EBL. There is flexibility in EBL where beam conditions can be changed under programmed controls to write low-resolution structures at higher speeds, although with reduced accuracy. To overcome this limitation, we demonstrated how a 'general purpose' optically defined structure in silicon with a resolution of ~microns was customized by SPL to define a high-resolution structure needed to produce a single electron transistor [87].

To summarize, low energy FE-SPL represents a promising alternative for patterning low-sensitive EBL resists. Since standard EBL achieved the highest resolution in in low sensitive resists, FE-SPL could be an appropriate replacement. Calixarene molecular glass is a resist on which FE-SPL exceeds the limits of standard EBL. In this context, FE-SPL is a promising tool for future rapid nanoscale manufacturing [85–87] and high-resolution nanoimprint lithography template fabrication [91, 93, 94].

Acknowledgments

The research leading to these results received funding from the European Union's Seventh Framework Programme FP7/2007-2013 under grant agreement no 318804 ('Single Nanometer Manufacturing for beyond CMOS devices'—acronym SNM). The authors also thank Tzvetan Ivanov from TU-Ilmenau for preparing the SPL-probes, Mathias Holz, and Alexander Reum from nano analytik GmbH, Ilmenau for the AFMin-SEM, and Christian Neuber from University of Bayreuth for fruitful discussions regarding molecular glass resist materials. The authors would like to express their sincerest thanks to Zahid Durrani and Mervyn Jones for the successful cooperation in the development of room-temperature single electron devices with the FE-SPL technology.

References

[1] Prati E and Shinada T 2013 *Single-Atom Nanoelectronics* (Singapore: Pan Stanford)
[2] Müller M, Fiedler T, Gröger R, Koch T, Walheim S, Obermair C and Schimmel T 2004 Controlled structuring of mica surfaces with the tip of an atomic force microscope by mechanically induced local etching *Surf. Interface Anal.* **36** 189–92
[3] Liu M Z, Amro N A and Liu G Y 2008 Nanografting for surface physical chemistry *Annu. Rev. Phys. Chem.* **59** 367–86
[4] Mamin H J and Rugar D 1992 Thermomechanical writing with an atomic force microscope tip *Appl. Phys. Lett.* **61** 1003–5
[5] Fenwick O, Bozec L, Credgington D, Hammiche A, Lazzerini G M, Silberberg Y R and Cacialli F 2009 Thermochemical nanopatterning of organic semiconductors *Nat. Nanotechnol.* **4** 664–8
[6] Torrey J D, Vasko S E, Kapetanovic A, Zhu Z H, Scholl A and Rolandi M 2010 Scanning probe direct-write of germanium nanostructures *Adv. Mater.* **22** 4639–42
[7] Jegadesan S, Sindhu S and Valiyaveettil S 2006 Easy writing of nanopatterns on a polymer film using electrostatic nanolithography *Small* **2** 481–4
[8] Marrian C R K, Dobisz E A and Dagata J A 1992 Electron-beam lithography with the scanning tunneling microscope *J. Vac. Sci. Technol.* B **10** 2877–81
[9] Park J, Park J Y, Choi T and Seo Y 2011 Graphite patterning in a controlled gas environment *Nanotechnology* **22** 335304
[10] Rangelow I W, Ivanov T, Sarov Y, Schuh A, Frank A, Hartmann H, Zöllner J P, Olynick D L and Kalchenko V 2010 Nanoprobe maskless lithography. *Proc. SPIE* **7637** 76370V
[11] Anderson E H, Olynick D L, Chao W L, Harteneck B and Veklerov E 2001 Influence of sub-100 nm scattering on high-energy electron beam lithography *J. Vac. Sci. Technol.* B **19** 2504–7
[12] Marrian C R K and Tennant D M 2003 Nanofabrication *J. Vac. Sci. Technol.* A **21** S207–15
[13] Cord B, Yang J, Duan H G, Joy D C, Klingfus J and Berggren K K 2009 Limiting factors in sub-10 nm scanning-electron-beam lithography *J. Vac. Sci. Technol.* B **27** 2616–21
[14] Grigorescu A E and Hagen C W 2009 Resists for sub-20-nm electron beam lithography with a focus on HSQ: state of the art *Nanotechnology* **20** 292001
[15] Walz M M, Vollnhals F, Rietzler F, Schirmer M, Steinruck H P and Marbach H 2012 Investigation of proximity effects in electron microscopy and lithography *Appl. Phys. Lett.* **100** 053118
[16] Manfrinato V R, Zhang L H, Su D, Duan H G, Hobbs R G, Stach E A and Berggren K K 2013 Resolution limits of electron-beam lithography toward the atomic scale *Nano Lett.* **13** 1555–8
[17] Manfrinato V R *et al* 2014 Determining the resolution limits of electron-beam lithography: direct measurement of the point-spread function *Nano Lett.* **14** 4406–12
[18] Manfrinato V R, Cheong L L, Duan H G, Winston D, Smith H I and Berggren K K 2011 Sub-5 keV electron-beam lithography in hydrogen silsesquioxane resist *Microelectron. Eng.* **88** 3070–4
[19] Greeneich J S 1980 Electron-beam processes *Electron-Beam Technology in Microelectronic Fabrication* ed G R Brewer (New York: Academic) pp 59–140
[20] Joy D C 1983 The spatial resolution limit of electron lithography *Microelectron. Eng.* **1** 103–19
[21] Schock K D, Prins F E, Strähle S and Kern D P 1997 Resist processes for low-energy electron-beam lithography *J. Vac. Sci. Technol.* B **15** 2323–6
[22] Wu B and Neureuther A R 2001 Energy deposition and transfer in electron-beam lithography *J. Vac. Sci. Technol.* B **19** 2508–11
[23] Joy D C 1995 A database on electron-solid interactions *Scanning* **17** 270–5
[24] De Vera P, Abril I and Garcia-Molina R 2011 Inelastic scattering of electron and light ion beams in organic polymers *J. Appl. Phys.* **109** 094901
[25] Tilke A, Vogel M, Simmel F, Kriele A, Blick R H, Lorenz H, Wharam D A and Kotthaus J P 1999 Low-energy electron-beam lithography using calixarene *J. Vac. Sci. Technol.* B **17** 1594–7

[26] Shirota Y 2005 Photo- and electroactive amorphous molecular materials - molecular design, syntheses, reactions, properties, and applications *J. Mater. Chem.* **15** 75–93

[27] Dai J Y, Chang S W, Hamad A, Yang D, Felix N and Ober C K 2006 Molecular glass resists for high-resolution patterning *Chem. Mater.* **18** 3404–11

[28] Fujita J, Ohnishi Y, Ochiai Y, Nomura E and Matsui S 1996 Nanometer-scale resolution of calixarene negative resist in electron beam lithography *J. Vac. Sci. Technol.* B **14** 4272–6

[29] Ishida M, J I F, Ogura T, Ochiai Y, Ohshima E and Momoda J 2003 Sub-10-nm-scale lithography using *p*-chloromethyl-methoxy-calix[4]arene resist *Jpn. J. Appl. Phys.* **42** 3913–6

[30] Solak H H, Ekinci Y, Kaser P and Park S 2007 Photon-beam lithography reaches 12.5 nm half-pitch resolution *J. Vac. Sci. Technol.* B **25** 91–95

[31] Ohnishi Y, Fujita J, Ochiai Y and S M 1997 Calixarenes-prospective materials for nanofabrication *Microelectron. Eng.* **35** 117–20

[32] Charlesby A 1960 *Atomic Radiation and Polymers* (Oxford: Pergamon)

[33] Perkins F K, Dobisz E A and Marrian C R K 1993 Determination of acid diffusion rate in a chemically amplified resist with scanning tunneling microscope lithography *J. Vac. Sci. Technol.* B **11** 2597–602

[34] Wilder K, Quate C F, Adderton D, Bernstein R and Elings V 1998 Noncontact nanolithography using the atomic force microscope *Appl. Phys. Lett.* **73** 2527–9

[35] Wilder K, Quate C F, Singh B and Kyser D F 1998 Electron beam and scanning probe lithography: a comparison *J. Vac. Sci. Technol.* B **16** 3864–73

[36] Ruderisch A 2003 *Synthese Von Calixaren- Und Resorcinarenderivaten Und Deren Anwendung in Chromatographie Und Nanotechnologie* (Tübingen: Eberhard-Karls-Universität Tübingen)

[37] Sailer H 2007 *Evaluierung Hochauflösender, Nicht Polymerer Elektronenstrahllacke Auf Calixaren–Basis* (Tübingen: Universitaet Tübingen)

[38] Prins F E, Pfeiffer J, Raible S, Kern D P and Schurig V 1998 Systematic studies of functionalized calixarenes as negative tone electron beam *Microelectron. Eng.* **41–2** 359–62

[39] De Oteyza D G, Perera P N, Schmidt M, Falch M, Dhuey S D, Harteneck B D, Schwartzberg A M, Schuck P J, Cabrini S and Olynick D L 2012 Sub-20 nm laser ablation for lithographic dry development *Nanotechnology* **23** 185301

[40] Perera P N, Schwartzberg A M, De Oteyza D G, Dhuey S D, Harteneck B D, Cabrini S and Olynick D L 2012 Selective laser ablation of radiation exposed methyl acetoxy calix(6)arene *J. Vac. Sci. Technol.* B **30** 06FI02

[41] Vorbringer-Doroshovets N *et al* 2013 0.1-nanometer resolution positioning stage for sub-10 nm scanning probe lithography *Proc. SPIE* **8680** 868018

[42] Kaestner M *et al* 2014 Scanning probes in nanostructure fabrication *J. Vac. Sci. Technol.* B **32** 06F101

[43] Heidenreich R D, Thompson L F, Feit E D and Melliar-Smith C M 1973 Fundamental aspects of electron beam lithography. I. Depth-dose response of polymeric electron beam resists *J. Appl. Phys.* **44** 4039–47

[44] Thompson L F, Feit E D, Melliar-Smith C M and Heidenreich R D 1973 Fundamental aspects of electron beam lithography. II. Low-voltage exposure of negative resists *J. Appl. Phys.* **44** 4048–51

[45] Vriens L 1966 Binary-encounter electron-atom collision theory *Phys. Rev.* **141** 88–92

[46] Vriens L 1966 Electron exchange in binary encounter collision theory *Proc. Phys. Soc.* **89** 13–21

[47] Kanik I, Trajmar S and Nickel J C 1992 Total cross section measurements for electron scattering on CH_4 from 4 to 300 eV *Chem. Phys. Lett.* **193** 281–6

[48] Giordan J C, Moore J H and Tossell J A 1986 Anion states of organometallic molecules and their ligands *Acc. Chem. Res.* **19** 281–6

[49] Kim Y K *et al* Electron-impact cross sections for ionization and excitation database (http://www.nist.gov/pml/data/ionization/index.cfm)

[50] Tanuma S, Powell C J and Penn D R 1990 Electron inelastic mean free paths in solids at low energies *J. Electron. Spectrosc. Relat. Phenom.* **52** 285–91

[51] Tanuma S, Powell C J and Penn D R 1992 Inelastic mean free paths of low-energy electrons in solids *Acta Phys. Pol.* A **81** 169–86

[52] Michaud M, Wen A and Sanche L 2003 Cross sections for low-energy (1-100 eV) electron elastic and inelastic scattering in amorphous ice *Radiat. Res.* **159** 3–22

[53] Mašín Z, Gorfinkiel J D, Jones D B, Bellm S M and Brunger M J 2012 Elastic and inelastic cross sections for low-energy electron collisions with pyrimidine *J. Chem. Phys.* **136** 144310

[54] Chang T H P, Kern D P and Muray L P 1992 Arrayed miniature electron beam columns for high throughput sub-100 Nm lithography *J. Vac. Sci. Technol.* B **10** 2743–8

[55] Silver C S, Spallas J P and Muray L P 2007 Multiple beam sub-80-nm lithography with miniature electron beam column arrays *J. Vac. Sci. Technol.* B **25** 2258–65

[56] Hordon L S, Huang Z R, Maluf N, Browning R and Pease R F W 1993 Limits of low-energy electron optics *J. Vac. Sci. Technol.* B **11** 2299–303

[57] Rangelow I W 2006 Scanning proximity probes for nanoscience and nanofabrication *Microelectron. Eng.* **83** 1449–55

[58] Rangelow I W, Ivanov T, Ahmad A, Kaestner M, Lenk C, Bozchalooi I S, Xia F Z, Youcef-Toumi K, Holz M and Reum A 2017 Review article: active scanning probes: a versatile toolkit for fast imaging and emerging nanofabrication *J. Vac. Sci. Technol.* B **35** 06G101

[59] Kaestner M *et al* 2015 Advanced electric-field scanning probe lithography on molecular resist using active cantilever *J. Micro/Nanolith. MEMS MOEMS* **14** 031202

[60] Fowler R H and Nordheim L 1928 Electron emission in intense electric fields *Proc. R. Soc.* A **119** 173–81

[61] Young R, Ward J and Scire F 1972 The topografiner: an instrument for measuring surface microtopography *Rev. Sci. Instrum.* **43** 999–1011

[62] Kragler K 1997 *Rastersondenlithographie Mit Niederenergetischen Elektronen* (Nürnberg: Friedrich-Alexander-Universität Erlangen-Nürnberg)

[63] Olynick D L *et al* 2015 Selective laser ablation in resists and block copolymers for high resolution lithographic patterning *J. Photopolym. Sci. Technol.* **28** 663–8

[64] Angelov T *et al* 2016 Six-axis AFM in SEM with self-sensing and self-transduced cantilever for high speed analysis and nanolithography *J. Vac. Sci. Technol.* B **34** 06KB01

[65] Wilson H A 1923 The motion of electrons in gases *Proc. R. Soc.* A **103** 53–57

[66] Kapzow N A 1955 *Elektrische Vorgänge in Gasen Und Im Vakuum* (Berlin: VEB Deutscher Verlag der Wissenschaften)

[67] Seah M P and Dench W A 1979 Quantitative electron spectroscopy of surfaces: a standard data base for electron inelastic mean free paths in solids *Surf. Interface Anal.* **1** 2–11

[68] Torok J *et al* 2013 Secondary electrons in EUV lithography *J. Photopolym. Sci. Technol.* **26** 625–34

[69] Denbeaux G *et al* 2013 Measurement of the role of secondary electrons in EUV resist exposures *Proc. Int. Workshop on EUV Lithography* (https://www.euvlitho.com/2013/P29.PDF)

[70] Marrian C R K, Dobisz E A and Colton R J 1990 Lithographic studies of an *e*-beam resist in a vacuum scanning tunneling microscope *J. Vac. Sci. Technol.* A **8** 3563–9
[71] Marrian C R K and Colton R J 1990 Low-voltage electron beam lithography with a scanning tunneling microscope *Appl. Phys. Lett.* **56** 755–7
[72] Dobisz E A, Marrian C R K and Colton R J 1990 Lithography with a 50 KV *e* beam and a vacuum scanning tunneling microscope in a polydiacetylene negative resist *J. Vac. Sci. Technol.* B **8** 1754–8
[73] Zhang L B, Shi J X, Yuan J L, Chang M and Wang X H 2003 The overview of scanning probe lithography by electron beam exposure of organic resists *Proc. 2003 3rd IEEE Conf. on Nanotechnology* (San Francisco, CA: IEEE) pp 797–800
[74] Lyuksyutov S F, Paramonov P B, Sharipov R A and Sigalov G 2004 Induced nanoscale deformations in polymers using atomic force microscopy *Phys. Rev.* B **70** 174110
[75] Ohto M, Yamaguchi S and Tanaka K 1995 Migration of metals on graphite in scanning tunneling microscopy *Japan. J. Appl. Phys.* **34** L694–7
[76] Leuschner R, Günther E, Falk G, Hammerschmidt A, Kragler K, Rangelow I W and Zimmermann J 1996 Bilayer resist process for exposure with low-voltage electrons (STM-lithography) *Microelectron. Eng* **30** 447–50
[77] Lenk C *et al* 2018 Experimental study of field emission from ultrasharp silicon, diamond, GaN, and tungsten tips in close proximity to the counter electrode *J. Vac. Sci. Technol.* B **36** 06JL03
[78] Kondo S, Heike S, Lutwyche M and Wada Y 1995 Surface modification mechanism of materials with scanning tunneling microscope *J. Appl. Phys.* **78** 155–60
[79] Kaestner M and Rangelow I W 2011 Scanning proximal probe lithography for sub-10 nm resolution on calix[4]resorcinarene *J. Vac. Sci. Technol.* B **29** 06FD02
[80] Krivoshapkina Y, Kaestner M, Lenk C, Lenk S and Rangelow I W 2017 Low-energy electron exposure of ultrathin polymer films with scanning probe lithography *Microelectron. Eng.* **177** 78–86
[81] Lyuksyutov S F, Vaia R A, Paramonov P B, Juhl S, Waterhouse L, Ralich R M, Sigalov G and Sancaktar E 2003 Electrostatic nanolithography in polymers using atomic force microscopy *Nat. Mater.* **2** 468–72
[82] Rangelow I W *et al* 2018 Atomic force microscope integrated with a scanning electron microscope for correlative nanofabrication and microscopy *J. Vac. Sci. Technol.* B **36** 06J102
[83] Holz M, Reuter C, Reum A, Ahmad A, Hofmann M, Ivanov T, Mechold S and Rangelow I W 2019 Atomic force microscope integrated into a scanning electron microscope for fabrication and metrology at the nanometer scale *Proc. SPIE* **11148** 111481F
[84] Holz M, Reuter C, Ahmad A, Reum A, Hofmann M, Ivanov T and Rangelow I W 2019 Correlative microscopy and nanofabrication with AFM integrated with SEM *Microsc. Today* **27** 24–30
[85] Holz M, F I A, Reuter C, Ahmad A, Hofmann M, Reum A, Ivanov T and Rangelow I W 2019 Tip-based electron beam induced deposition using active cantilevers *J. Vac. Sci. Technol.* B **37** 061812
[86] Rangelow I W *et al* 2016 Pattern-generation and pattern-transfer for single-digit Nano devices *J. Vac. Sci. Technol.* B **34** 06K202
[87] Durrani Z, Jones M, Abualnaja F, Wang C, Kaestner M, Lenk S, Lenk C, Rangelow I W and Andreev A 2018 Room-temperature single dopant atom quantum dot transistors in silicon, formed by field-emission scanning probe lithography *J. Appl. Phys.* **124** 144502
[88] Kaestner M, Hofer M and I W R 2013 Nanolithography by scanning probes on calixarene molecular glass resist using mix-and-match lithography *J. Micro/Nanolith. MEMS MOEMS* **12** 031111
[89] Kaestner M and I W R 2012 Multi-step scanning probe lithography (SPL) on calixarene with overlay alignment *Proc. SPIE* **8323** 83231G
[90] Tennant D M 1999 Limits of conventional lithography *Nanotechnology* ed G Timp (Berlin: Springer) pp 161–205
[91] Lenk C *et al* 2019 High-throughput process chain for single electron transistor devices based on field-emission scanning probe lithography and Smart Nanoimprint lithography technology *J. Vac. Sci. Technol.* B **37** 021603
[92] Rangelow I W *et al* 2017 Single Nano-digit and closed-loop scanning probe lithography for manufacturing of electronic and optical nanodevices *Proc. SPIE* **10456** 1045621
[93] Rangelow I W *et al* 2018 Field-emission scanning probe lithography with self-actuating and self-sensing cantilevers for devices with single digit nanometer dimensions *Proc. SPIE* **10584** 1058406
[94] Holz M *et al* 2018 Field-emission scanning probe lithography tool for 150 mm Wafer *J. Vac. Sci. Technol.* B **36** 06JL06